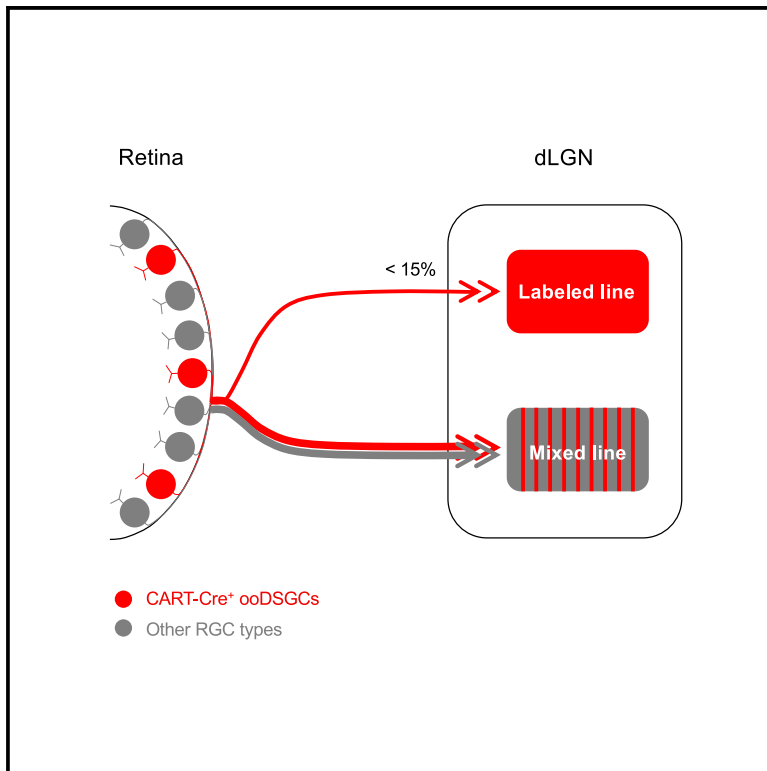


Functional convergence of on-off direction-selective ganglion cells in the visual thalamus

Graphical abstract



Authors

Qiufen Jiang, Elizabeth Y. Litvina,
Héctor Acarón Ledesma,
Guanhua Shu, Takuma Sonoda,
Wei Wei, Chinfai Chen

Correspondence

chinfai.chen@childrens.harvard.edu

In brief

Jiang and Litvina et al. explore the rules of convergence among inputs from different types or subtypes of RGCs onto thalamocortical neurons in visual thalamus. They identify a specific wiring organization for on-off direction-selective retinal inputs. Their results show that distinct rules apply for RGC types versus subtypes.

Highlights

- Most relay (TC) neurons innervated by ooDSGCs receive inputs from other RGC types
- Only a small fraction of TC neurons are primarily driven by ooDSGCs
- TC neurons tend not to receive both inputs from ventrally and dorsally tuned ooDSGCs

Article

Functional convergence of on-off direction-selective ganglion cells in the visual thalamus

Qiufen Jiang,^{1,4} Elizabeth Y. Litvina,^{1,2,4} Héctor Acarón Ledesma,¹ Guanhua Shu,¹ Takuma Sonoda,¹ Wei Wei,³ and Chinfei Chen^{1,5,*}

¹F.M. Kirby Neurobiology Center, Boston Children's Hospital, Harvard Medical School, 3 Blackfan Circle, Boston, MA 02115, USA

²National Institute of Neurological Disorders and Stroke, 6001 Executive Boulevard Suite 3309, Bethesda, MD 20824, USA

³Department of Neurobiology, The University of Chicago, 947 East 58th Street, Chicago, IL 60637, USA

⁴These authors contributed equally

⁵Lead contact

*Correspondence: chinfei.chen@childrens.harvard.edu

<https://doi.org/10.1016/j.cub.2022.06.023>

SUMMARY

In the mouse visual system, multiple types of retinal ganglion cells (RGCs) each encode distinct features of the visual space. A clear understanding of how this information is parsed in their downstream target, the dorsal lateral geniculate nucleus (dLGN), remains elusive. Here, we characterized retinogeniculate connectivity in *Cart-IRES2-Cre-D* and *BD-CreER2* mice, which labels subsets of on-off direction-selective ganglion cells (ooDSGCs) tuned to the vertical directions and to only ventral motion, respectively. Our immunohistochemical, electrophysiological, and optogenetic experiments reveal that only a small fraction (<15%) of thalamocortical (TC) neurons in the dLGN receives primary retinal drive from these subtypes of ooDSGCs. The majority of the functionally identifiable ooDSGC inputs in the dLGN are weak and converge together with inputs from other RGC types. Yet our modeling indicates that this mixing is not random: *BD-CreER2*⁺ ooDSGC inputs converge less frequently with ooDSGCs tuned to the opposite direction than with non-CART-Cre⁺ RGC types. Taken together, these results indicate that convergence of distinct information lines in dLGN follows specific rules of organization.

INTRODUCTION

Understanding the circuit mechanisms underlying the integration of information in the central nervous system has been key to progress in neuroscience. An emerging experimental model for studying this question is the mouse retinogeniculate synapse: the connection between retinal ganglion cells (RGCs) in the eye and thalamocortical (TC) relay neurons in the visual thalamus. In mice, at least 40 distinct types of RGCs encoding different visual features have been described based on their unique combination of morphological, genetic, and physiological properties.^{1–7} One prominent feature of the mouse retina is the on-off direction-selective circuit in which the output neurons, the on-off direction-selective ganglion cells (ooDSGCs), respond to both increments and decrements of light and fire maximally to motion along one particular direction. ooDSGCs comprise about 15% of the total RGC population^{8,9} and can be classified into 4 subtypes, each tuned to one of four cardinal axes: dorsal (downward in visual field), ventral (upward), nasal (posterior), or temporal (anterior).^{3,9–12} ooDSGCs play a fundamental role in detecting alterations in light intensity and stimulus motion that is critical for behavior.^{4,13}

In mice, ooDSGCs project to the dorsal lateral geniculate nucleus (dLGN) in the image-forming pathway, raising questions

of whether and how this information is parsed on its way to the cortex. The traditional view is that visual information is relayed from retina to cortex along “labeled lines,” such that the feature selectivity of an RGC type matches that of the TC neuron it innervates.^{14,15} However, recent studies have shown that RGC inputs with different features can converge onto the same TC neuron, implying a greater degree of integration in this thalamic “relay station” than previously recognized.^{16–19} Little is known of how the synaptic organization of ooDSGCs in the dLGN maps onto these two opposing schema: evidence that ooDSGC signals can both occupy distinct “labeled lines” and integrate with other retinal information streams has been reported.^{16,19} However, these studies focused on presynaptic activity or rabies virus labeling, rather than directly assessing synaptic function. Here, we took advantage of available genetic tools to examine both the anatomical and functional relevance and the relative prevalence of these two schema using optogenetics to identify ooDSGC inputs.

To determine whether inputs that are tuned to different directions exhibit similar synaptic properties and weights, we take advantage of two Cre-expressing transgenic mouse lines that identify different subtypes of ooDSGCs, one a subset of the other. The cocaine- and amphetamine-regulated transcript neuropeptide (CART; gene symbol *Cartpt*) is selectively expressed in

three ooDSGC subtypes tuned to dorsal, ventral, or nasal motion.^{8,20} The *Cart-IRES2-Cre-D* mouse line was therefore used to simultaneously label multiple subtypes of ooDSGCs.¹² The *BD-CreER* mouse is a tamoxifen-dependent line that labels one subtype of this population: ooDSGCs tuned to ventral motion in the retina. In this study, we characterize and compare the anatomical and synaptic properties of these two sets of ooDSGCs in the dLGN. Axon labeling analysis and electrophysiological studies reveal that these two sets make functional connections in the same region of the dLGN. However, *BD-CreER*⁺ inputs tend not to converge onto the same post-synaptic TC neurons with the other (oppositely tuned) *CART-Cre*⁺ ooDSGC inputs. Instead, *CART-Cre*⁺ or *BD-CreER*⁺ ooDSGC inputs preferentially converge with other RGC-type inputs. Moreover, only a small fraction of TC neurons receive more than 50% of their drive from *BD-CreER*⁺ or *CART-Cre*⁺ inputs. Our findings suggest that there are specific rules for the convergence of information lines coding distinct aspects of the visual space.

RESULTS

Specific expression of ChR2 in *CART*⁺ RGCs

To assess the functional contributions of distinct ooDSGCs in the dLGN, we aimed to selectively label axons of RGC subsets tuned to different directions.^{2,8} Of the different available *Cart-Cre* mouse lines, we characterized *Cart-IRES2-Cre-D* ("*Cart-Cre*") by crossing the line with Cre-dependent GCaMP6f mice (*Ai95D*). Calcium responses to bars moving along eight directions were recorded from *CART-Cre*⁺ RGCs expressing GCaMP6f (Figure 1A; STAR Methods). *Cart-Cre* mainly label ooDSGCs tuned to the vertical directions with 50.6% preferring dorsal and 49.4% preferring ventral motion (Figures 1B and S1). By contrast, *BD-CreER*⁺ RGCs have been previously characterized as labeling just one *CART*⁺ RGC subtype, tuned to ventral motion.^{8,21} We therefore chose these two lines for further studies.

We next assessed channelrhodopsin-2 (ChR2) expression in retinas of P30 *Cart-Cre* or *BD-CreER* mice crossed with Cre-dependent ChR2-EYFP-expressing mice, *Ai32* (termed "*Cart;ChR2*" and "*BD;ChR2*" mice, respectively). Consistent with previous reports, immunostaining demonstrated labeling of assorted retinal cells, including RGCs, glial cells, and putative amacrine cells, in the *Cart;ChR2* retinas (Figure 1C₁, left).^{2,22} As only RGCs project out of the retina to the dLGN, we focused on the specificity of the *Cart;ChR2* RGC-type labeling, using RBPMs to identify RGCs. In *Cart;ChR2* mice, 91.46% ± 2.33% of GFP⁺ (*CART-Cre*⁺) RGCs in the ganglion cell layer co-immunostained with *CART* (n = 4 mice), demonstrating a high degree of specificity of ChR2 labeling (Figure 1C₂, left). However, only approximately half (53.92% ± 1.07%) of *CART*-immunoreactive (*CART*⁺) RGCs (RBPMs⁺) expressed GFP (Figure 1C₂, right), consistent with our finding that *Cart;ChR2* labels only the subtypes of *CART*-expressing ooDSGCs preferring vertical motion (Figure 1B) and that dorsally and ventrally tuned ooDSGCs comprise ~50% of all *CART*⁺ RGCs.¹²

A similar analysis in the retina of *BD;ChR2* mice revealed a high proportion of GFP⁺ (*BD-CreER*⁺) RGCs that expressed *CART* (93.82% ± 1.84%, n = 5 mice) (Figures 1D₁ and 1D₂, left), consistent with *BD* RGCs being a subtype of *CART* ooDSGCs. Among

the *CART*⁺ RGCs, 34.59% ± 3.72% expressed GFP in the retina of *BD;ChR2* mice (Figure 1D₂, right). Due to a lack of antibodies specific for labeling *BD* RGCs, we were not able to quantify the efficiency of ChR2 labeling in *BD* RGCs. Overall, these data demonstrated that ChR2 expression among axons leaving the retina in both mouse lines is largely restricted to ooDSGCs.

To discern labeling of retinal projections from other potential sources, we examined co-localization of ChR2-tagged GFP and VGlut2 (a presynaptic marker for RGC inputs²³) in the dLGN. In both mouse lines, GFP⁺ axonal boutons exhibit a high degree of overlap with VGlut2 immunostaining (Figure 1E). Furthermore, binocular enucleation completely removed ChR2 labeling from dLGN for both mouse lines (Figure 1F), indicating that the retina is its sole source. Together, these data support the use of *Cart;ChR2* and *BD;ChR2* mice to selectively label, activate, and compare the TC neuron response to these two sets of *CART*⁺ ooDSGCs inputs.

Anatomical organization of *CART-Cre*⁺ and *BD-CreER*⁺ inputs in the dLGN

We next compared RGC axonal territories in the dLGN of the two mouse lines. In coronal sections of the dLGN of *Cart;ChR2* mice, GFP⁺ RGC axons could be observed to terminate densely in the dorsal aspect bordering the ventricle and to extend deeper into the nucleus when moving along the anterior-posterior axis (Figure 2A, left). The axonal labeling of GFP⁺ RGCs from *BD;ChR2* mice overlapped largely with the territory of *CART-Cre*⁺ terminals with the exception of the most dorsal edge of the dLGN (Figure 2A, right). To compare the spatial distribution of terminal endings between *CART-Cre*⁺ and *BD-CreER*⁺ axons, we collapsed the two-dimensional dLGN area into a one-dimensional line plot by summing the signals of maximal intensity projections along the lateral-to-medial axis of the coronal slice (Figure S2B, top; STAR Methods). The line plots confirmed the overlap of spatial territory between *CART-Cre*⁺ and *BD-CreER*⁺ inputs in a deeper area of dLGN, as expected, given that *BD-CreER*⁺ RGCs comprise a subset of *CART-Cre*⁺ ooDSGCs (Figure S2B, bottom). Taken together, when compared with the distribution of axonal terminals in *Cart;ChR2* mice, *BD-CreER*⁺ inputs were sparser and concentrated in a subregion of the occupied territory.

Functional organization of *CART-Cre*⁺ and *BD-CreER*⁺ inputs in dLGN

Our Figure 2 and published^{2,8,26-29} data indicate that both *CART* and *BD* RGCs preferentially project to dLGN "shell" region. Since retinal inputs synapse on the proximal dendrites of TC neurons,^{17,30-35} the anatomical distribution of RGC axons in dLGN should map well with the distribution of functional inputs onto TC neurons. Thus, we examined the functional connectivity of *CART-Cre*⁺ and *BD-CreER*⁺ ooDSGCs in their overlapping territory in the dLGN. To assess the strength and spatial distribution of retinogeniculate drive from *CART-Cre*⁺ and *BD-CreER*⁺ RGCs, we used an established parasagittal slice preparation of the dLGN (STAR Methods), optimized for physiology because it preserves the retinal axon arbors.³⁶⁻³⁸ We first compared the expression of ChR2 from this parasagittal view and found that *BD-CreER*⁺ terminals overlap with a subset of

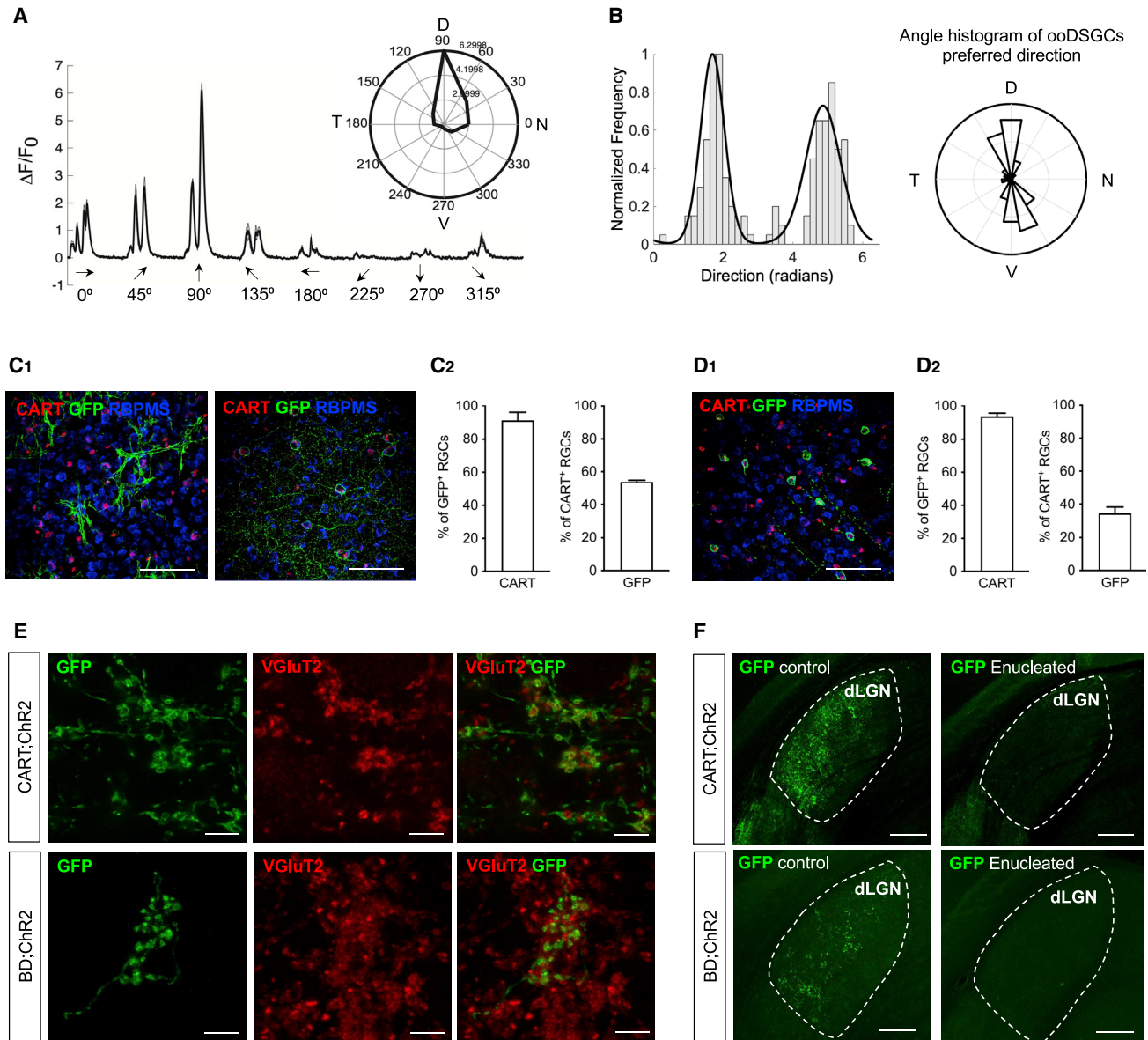


Figure 1. Specific expression of Chr2 in CART⁺ RGCs

(A) Representative example of calcium responses to moving bars along 8 directions from one CART-Cre⁺ RGC tuned to dorsal motion. Inset: polar plot. (B) Tuning distribution of CART-Cre⁺ oDSGCs (n = 246 cells from 12 retinas, 8 mice). Left: normalized frequency distribution, fit by a mixture of two Gaussian distributions (black line). Right: polar plot distribution showing that labeled RGCs are mainly tuned to dorsal and ventral motions. See also Figure S1. (C) Representative images from the RGC layer of *Cart;Chr2* mouse retina immunostained for GFP (green, ChR2-EYFP), RBPMS (blue, RGCs), and CART (red, oDSGCs) (n = 4 mice). (C₁) Left: glial cells are labeled in the *Cart;Chr2* mouse. Right: subsets of RGCs also express Chr2. (C₂) Left: CART immunostaining in ChR2-expressing RGCs. Right: Chr2 expression in CART⁺ RGCs. (D) As in (C) but for *BD;Chr2* mouse retina (n = 5 mice). (E) Confocal images of ChR2-expressing axonal boutons in the dLGN co-immunostained for GFP and vGluT2 in *Cart;Chr2* (top) and *BD;Chr2* (bottom) mice. (F) ChR2-expressing axonal boutons in the dLGN of enucleated mice. Left: normally reared mice. Right: bilaterally enucleated mice (*STAR Methods*) from *Cart;Chr2* (top, n = 3) and *BD;Chr2* mice (bottom, n = 3). Scale bars, 100 μm in (C) and (D), 5 μm in (E), and 200 μm in (F).

CART-Cre⁺ terminals in the ventral-posterior territory (Figures 2B and S2C; *STAR Methods*).

Then we performed whole-cell patch-clamp recordings of randomly sampled TC neurons from the ventral-posterior area (Figure 2B, lateral and middle sections). We recorded maximal

excitatory post-synaptic currents, optically evoked using full-field blue light illumination (oEPSCs) (Figure 3A) and by adding bicuculline (GABA_AR antagonist), CGP55845 (GABA_BR antagonist), DPCPX (antagonist of A1 adenosine receptors), and LY341495 (antagonist of presynaptic group II mGluRs) in the

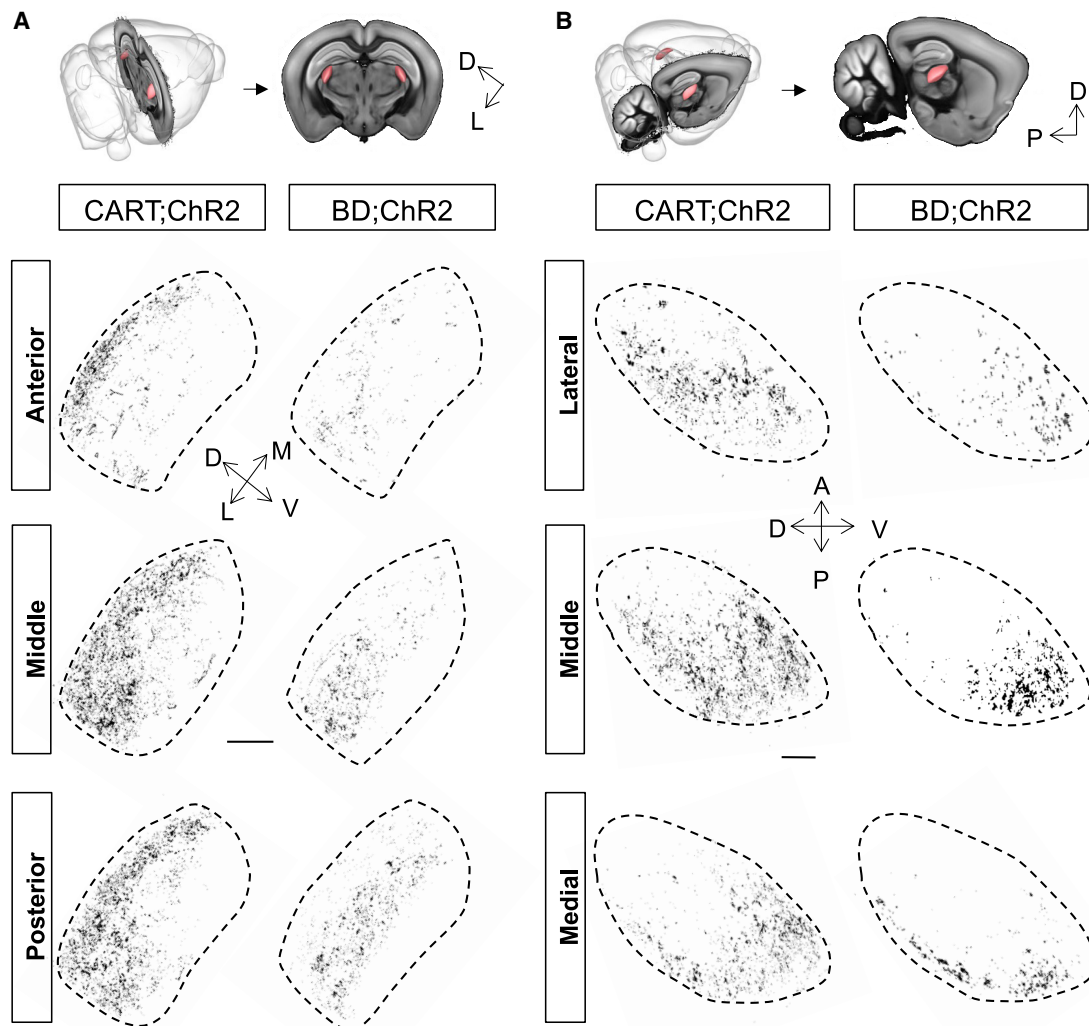


Figure 2. Distinct terminal labeling of CART-Cre⁺ and BD-CreER⁺ RGC axons in the dLGN

(A) Distribution of ChR2-expressing axons in coronal dLGN sections. Top: schematic for coronal slices (from Scalable Brain Atlas;^{24,25} STAR Methods). Bottom: coronal slices from anterior, middle, and posterior dLGN of *Cart;ChR2* (left, n = 3 mice) and *BD;ChR2* (right, n = 3) mice.

(B) Like (A) but from parasagittal sections from lateral, middle, and medial dLGN (n = 3 mice each for *Cart;ChR2* and *BD;ChR2* mice). Scale bars, 200 μ m. See also Figure S2 and STAR Methods.

bath solution (STAR Methods).^{39,40} The ratio of AMPA receptor (AMPA)/NMDA receptor (NMDAR) currents between CART-Cre⁺ and BD-CreER⁺ inputs did not differ (CART, 1.15 ± 0.09 , n = 61; BD, 1.36 ± 0.11 , n = 52; Mann-Whitney test, p = 0.054), indicating comparable developmental maturation of RGC inputs labeled by the two mouse lines. Nor did tamoxifen injections in *BD;ChR2* significantly alter the function or development of the retinogeniculate synapse (Figure S3B; STAR Methods).

TC neurons can receive inputs from multiple different types of RGCs.^{16,17,41,42} To begin to understand how the diversity of oDSGCs maps onto these convergence patterns, we examined the amplitude of oEPSCs resulting from the activation of CART-Cre⁺ or BD-CreER⁺ RGCs. In our recording conditions, peak AMPAR currents smaller than 600 pA cannot drive the firing of TC neurons alone in response to a single stimulus.⁴³ We therefore used this amplitude threshold to sort the oEPSCs we recorded into “weak” (<600 pA) and “strong” (>600 pA) inputs.

We further categorized “strong” inputs that were greater than 2,000 pA as “dominant” inputs since our previously published study showed that simultaneous activation of all retinal inputs generally evokes oEPSCs that exceed this value in *Chx10;ChR2* mice⁴¹ (*Chx10* is expressed in all RGCs; Figures 3B and 3D). Recordings do not distinguish oEPSCs elicited from single versus multiple contributing RGCs. Therefore, oEPSCs correspond to the maximal summed responses of all ChR2⁺ CART or BD RGCs synapsing onto an individual TC neuron. Most of these maximal responses were weaker than 600 pA for both CART-Cre⁺ ($69.59\% \pm 7.35\%$, n = 74 cells from 9 mice) and BD-CreER⁺ inputs ($62.44\% \pm 7.11\%$, n = 60 cells from 35 mice) (Figures 3C and 3E).

We next asked whether or not CART-Cre⁺ and BD-CreER⁺ inputs drive spatially distinct populations of TC neurons within this area or whether weak versus strong inputs are spatially segregated. We superimposed a grid over the parasagittal slice of

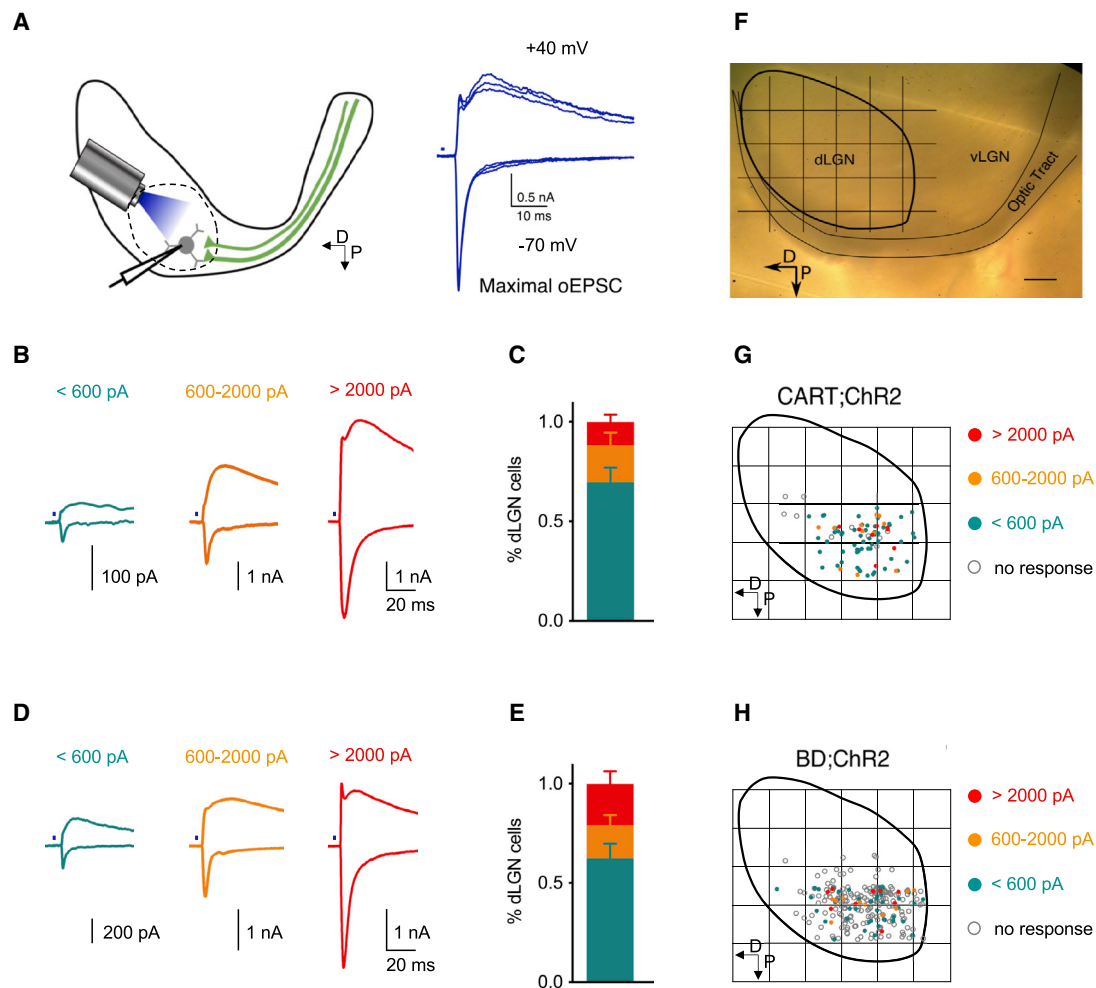


Figure 3. Synaptic properties and spatial distribution of *CART-Cre*⁺ and *BD-CreER*⁺ inputs

(A) Experimental protocol. Left: schematic diagram of oEPSC recordings obtained from TC neurons located in ventral-posterior region outlined by dashed curve. Right: example traces of maximal AMPAR and NMDAR oEPSC (holding potential -70 and $+40$ mV, respectively).

(B) Example traces of maximal *CART-Cre*⁺ oEPSCs classified in three groups based on amplitude: less than 600 pA, large amplitude between 600 and $2,000$ pA, and dominant inputs larger than $2,000$ pA. The traces are color coded for classification in (C) and (G).

(C) Distribution of *CART-Cre*⁺ AMPAR oEPSC amplitudes ($n = 74$ cells from 9 mice).

(D and E) Same as (B) and (C) for maximal *BD-CreER*⁺ oEPSCs ($n = 60$ cells from 35 mice).

(F) Grid superimposed over dLGN image allows mapping of the approximate location of recorded neurons. Scale bars, $200 \mu\text{m}$.

(G and H) Spatial distribution of *CART-Cre*⁺ ($n = 93$ cells) and *BD-CreER*⁺ responses ($n = 318$ cells).

See also [Figure S3](#) and [STAR Methods](#).

the dLGN as a reference ([Figure 3F](#)) and tabulated the approximate location of each recorded TC neuron while color coding the strength of their AMPAR oEPSC ([Figures 3G](#) and [3H](#)). Unresponsive neurons (those without a measurable oEPSC) were also annotated. In the region of axonal overlap from the two mouse lines, we found no discernable spatial pattern in TC neurons based on their responsiveness or oEPSC strength in *Cart;ChR2* mice ([Figures 3G](#), [S3D](#), and [S3E](#), left; two-way ANOVA, $p = 0.64$). Moreover, TC neurons driven by *BD-CreER*⁺ RGCs are not spatially segregated from those by *CART-Cre*⁺ RGCs within the ventral-posterior territory ([Figures 3H](#) and [S3E](#), right; two-way ANOVA, $p = 0.71$).

Our finding of distinct regions in the dLGN that appear to receive *BD-CreER*⁺ inputs and/or *CART-Cre*⁺ raised the

question of whether ooDSGC-preferring dorsal motion (labeled by *Cart;ChR2* but not *BD;ChR2* mice) exclusively innervate dLGN regions distinct from those preferring ventral motion ooDSGCs (labeled by *BD;ChR2* mice).⁴⁴ However, this scenario could not explain our findings in [Figures 3G](#) and [3H](#). Far more sampled TC neurons were innervated by *CART-Cre*⁺ inputs ($\sim 89\%$) than by *BD-CreER*⁺ inputs ($\sim 24\%$) ([Figures 3G](#) and [3H](#)). This difference cannot be simply explained by inefficient labeling in *BD;ChR2* mice, since *BD-CreER*⁺ RGCs and *CART-Cre*⁺ RGCs comprise $\sim 35\%$ and $\sim 54\%$ of *CART*⁺ RGCs, respectively, in the retina ([Figures 1C₂](#) and [1D₂](#), right). Taken together, our findings suggest that *CART-Cre*⁺ inputs terminating in the ventral-posterior area of dLGN cannot arise just from ooDSGCs tuned to ventral motion, but that *CART-Cre*⁺ inputs

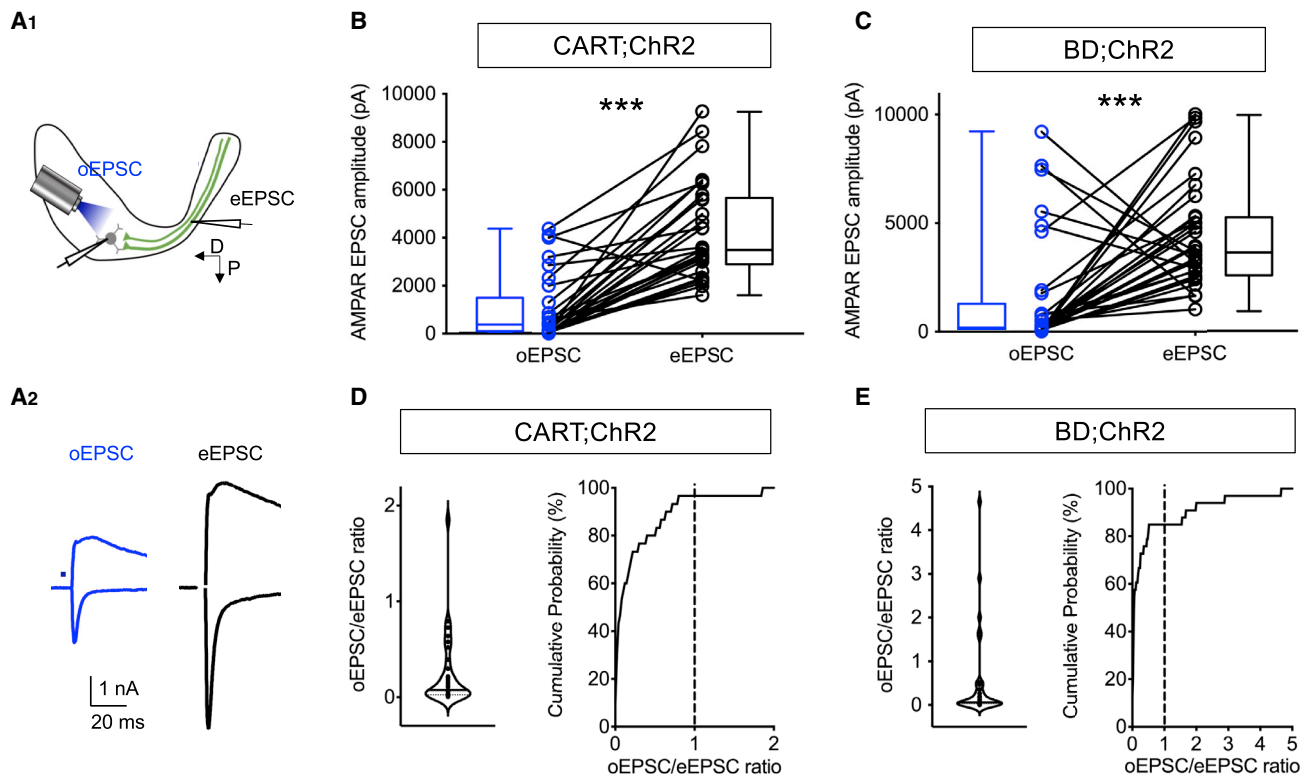


Figure 4. Contribution of CART-Cre⁺ and BD-CreER⁺ inputs to total retinal drive

(A) Recording of maximal oEPSCs and electrical EPSCs (eEPSCs). (A₁) Schematic diagram. (A₂) Example traces of maximal oEPSC and eEPSC from the same cell.

(B and C) Comparison of maximal AMPAR oEPSCs to eEPSCs from the same TC neuron for CART-Cre⁺ inputs (n = 30 cells, 9 mice) and BD-CreER⁺ inputs (n = 33 cells, 19 mice). ***p < 0.001, Wilcoxon matched-pairs signed-rank test.

(D and E) Median distribution of oEPSC/eEPSC ratio in the two mouse lines. Left: violin plot of oEPSC/eEPSC ratio, with median indicated by solid line and quartiles by dashed lines. Right: cumulative probability distribution of oEPSC/eEPSC ratio, where primary drivers are defined as inputs with oEPSC/eEPSC > 1 (vertical dashed line: ratio = 1).

tuned to both ventral and dorsal motions must co-innervate this region. Therefore, axons from ooDSGCs tuned to two opposite directions appear broadly distributed across the same area.

Contribution of CART-Cre⁺ and BD-CreER⁺ RGCs to the total retinal drive of TC neurons

We next estimated the contribution of CART-Cre⁺ or BD-CreER⁺ inputs to the total retinal drive by comparing maximal amplitudes of CART/BD oEPSCs to electrical EPSCs (eEPSCs) from the same TC neuron (Figure 4A). The eEPSC reflects the synaptic response to the stimulation of axons from a mixed set of RGC types. In both *Cart;Chr2* and *BD;Chr2* mice, the amplitude of oEPSCs was substantially smaller than that of eEPSCs (CART, n = 30 cells, p < 0.001; BD, n = 33 cells, p < 0.001; non-parametric Wilcoxon matched-pairs signed-rank test; Figures 4B and 4C). The median ratios of oEPSC to eEPSC amplitude were 0.075 (IQR: 0.297) for CART-Cre⁺ inputs and 0.057 (IQR: 0.38) for BD-CreER⁺ inputs (Figures 4D and 4E, left). Factoring in the loss of axonal continuity in the slice preparation (ratio of *Chx10;Chr2* evoked oEPSC/eEPSC = ~2),⁴¹ we defined CART⁺/BD⁺ inputs as primary drivers when the inputs contribute to more than 50% of total retinal drive, that is, when oEPSC/eEPSC ratio is equal to or greater than 1 (STAR Methods). Using

this criterion, we observed that the majority of TC neurons receive only weak ooDSGC innervation (CART, 96.67%; BD, 84.85%; Figures 4D and 4E, right). These data suggest that CART-Cre⁺ and BD-CreER⁺ inputs most frequently converge onto TC neurons in which the majority of their additional inputs are from other RGC types.

Role of Chr2-expression efficiency in convergence analyses

We remained concerned that the small amplitude of most ooDSGCs inputs might reflect insufficient penetrance of Chr2 expression in the two ooDSGC populations. To test this possibility, we compared the cumulative probability distributions of CART-Cre⁺ or BD-CreER⁺ oEPSCs with eEPSCs amplitudes, with each curve normalized to its respective population maximal oEPSC or eEPSC current. We reasoned that, even if only a small subset of vertical ooDSGC axons can be activated optogenetically, the overall cumulative distribution of optically driven responses should resemble that of eEPSCs and should align when normalized. In fact, these normalized plots showed that the distribution of CART-Cre⁺ and BD-CreER⁺ oEPSCs was shifted to the left and had a different shape when compared with that of eEPSCs (Figures 5A and

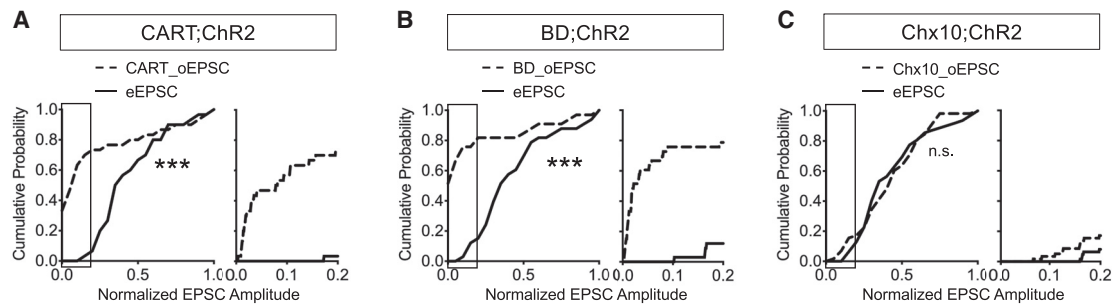


Figure 5. Comparison of amplitude distributions for different RGC inputs

Cumulative probability distribution of oEPSC and eEPSC amplitudes (normalized to the maximal current in each respective group) for CART-Cre⁺ (A) (n = 30 cells), BD-CreER⁺ (B) (n = 33 cells), and Chx10-Cre⁺ (C) (n = 58 cells, from data obtained from Litvina and Chen⁴¹). Right: expanded amplitude scale corresponding to the box in the left panel. ***p < 0.001; n.s., p = 0.65; Kolmogorov-Smirnov test.

5B; Kolmogorov-Smirnov [K-S] test, p < 0.001). By contrast, the curve of the responses to bulk optogenetic stimulation of retinal inputs (*Chx10;ChR2*; previously published⁴¹) is very similar to that of the eEPSC (Figure 5C; K-S test, p = 0.65). These results indicate non-uniform contributions of ooDSGC inputs across the population of TC neurons and support the idea that, for the majority of TC neurons, retinal inputs recruited by electrical stimulation are not all drawn from a population of CART-Cre⁺ or BD-CreER⁺ RGCs inputs; in fact, they rather suggest an integration between ooDSGC and non-ooDSGC inputs.

Logic for wiring on-off directional inputs in the dLGN

At the level of an individual TC neuron dendrite, retinal boutons preferentially cluster together when their preferred directions are very similar and, more rarely, opposite to one another.¹⁹ Here, we asked whether synapses of ventral-preferring BD RGCs converge onto a given TC neuron with those of CART RGCs tuned to the opposite direction. To begin to address this question, we explored models of two opposite potential wiring patterns between the two CART-Cre⁺ ooDSGC subsets and TC neurons: (1) TC neurons are innervated by convergent CART-Cre⁺ RGC subsets that code for two different directions (model A, Figure 6A₁), or (2) TC neurons exclusively receive inputs from one CART-Cre⁺ RGC subset that codes for a specific direction (model B, Figure 6A₂). Accordingly, the inputs from each subset and total CART-Cre⁺ RGCs were simulated based on these two models (STAR Methods). We assumed that cumulative amplitude histograms of ooDSGCs preferring ventral versus dorsal motion are very similar and can be represented by that for BD-CreER⁺ inputs. Model A predicts that the cumulative curve of CART inputs will be significantly shifted to the right of that of BD inputs (Figure 6B₁; K-S test, p < 0.001). In model B, each individual TC neuron receives inputs from only one subtype of ooDSGCs; thus, the distribution of synaptic responses to CART-Cre⁺ ooDSGC inputs would be very similar to that of the ooDSGC subtype tuned to ventral motion. Our experimental data were more consistent with model B as the distributions from the two lines were statistically indistinguishable (Figure 6C). Moreover, the distribution of CART-Cre⁺ inputs predicted by model A (but not model B) significantly differs from that of experimental CART-Cre⁺ responses (versus data: model A,

p < 0.0005; model B, p = 0.67; K-S test with Bonferroni correction).

We also modeled the impact of possible contamination of the oEPSCs in *Cart-Cre* with other RGC types (Figure S1C; 27% non-specifically labeled RGCs that may or may not also project to the sampled dLGN region). For model A, the non-ooDSGC RGCs labeled in *Cart;ChR2* mice may converge with both CART-Cre⁺ ooDSGC subtypes (Figure S4A1) or target a distinct set of TC neurons (Figure S4B1). Simulations of these scenarios yielded significantly different cumulative distribution curves between CART and BD inputs (Figures 6A₂ and 6B₂; K-S test, p < 0.001). Similarly, for model B, labeled non-ooDSGCs may mix with both subtypes of vertically tuned ooDSGCs (Figure S4C1) or innervate a distinct group of TC neurons, compared with CART-Cre⁺ ooDSGCs (Figure S4D1). Our simulation for the former still predicts a shift in the distribution of CART-Cre⁺ inputs when compared with BD inputs (Figure 6C2; K-S test, p < 0.001). On the contrary, the latter yielded a similar cumulative distribution between vertically tuned ooDSGC inputs and ventral motion-preferring inputs (Figure 6D₂), consistent with functional recordings. Taken together, our data argue that the likelihood of BD-CreER⁺ inputs converging onto the same TC neuron with the ooDSGCs preferring the opposite direction (dorsal) appears to be low.

DISCUSSION

In mice, neurons tuned to motion information are found in the retina, dLGN, and V1.^{28,45–51} Additionally, direction and orientation selectivity have been shown to be computed *de novo* in the visual cortex. How these different streams of information interact is a subject of active investigation.^{50–52} To address this question, a basic understanding of how motion information from the retina is parsed in dLGN is essential. Motion selectivity in TC neurons could be inherited from the eye, consistent with a labeled line model and observations in superior colliculus,⁵³ or computed *de novo* in the dLGN. Consistent with the latter, different information streams can converge onto the same TC neuron.^{16,18,19} The logic of which RGC types do or do not converge and the relative strengths of these inputs are still unclear. Here, we took advantage of two *Cre* mouse lines, one labeling a subset population of the other, to identify and drive ooDSGCs inputs tuned to ventral

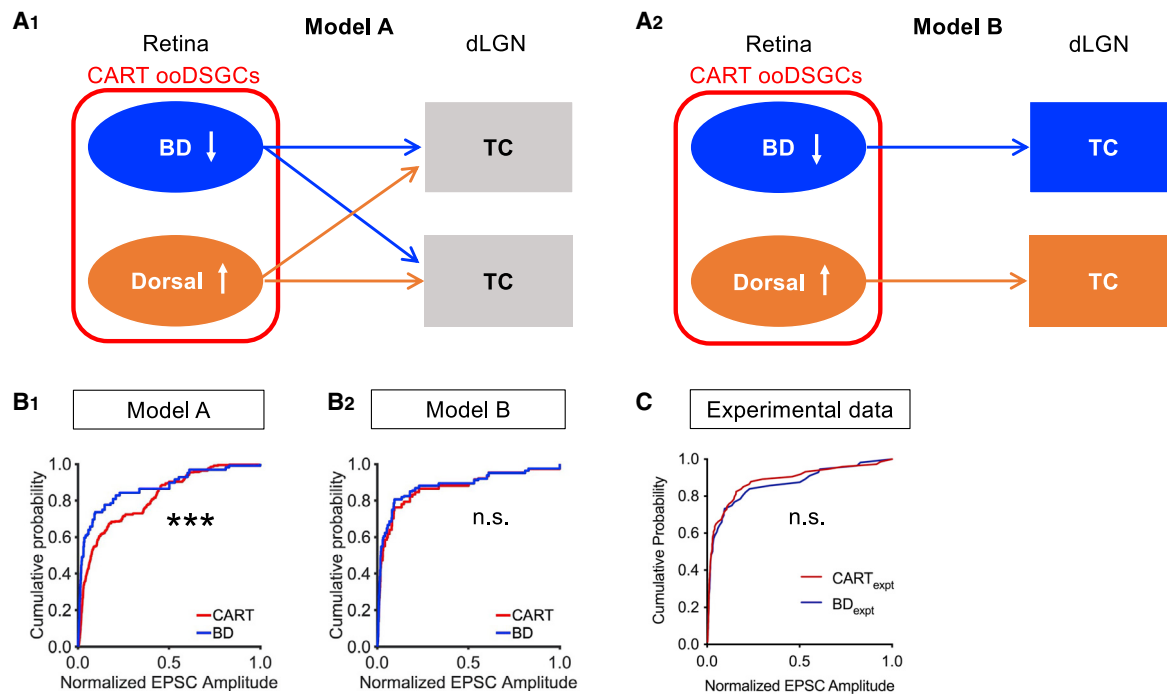


Figure 6. Modeling convergence of CART-Cre⁺ and BD-CreER⁺ inputs in the dLGN

(A) Possible models of innervation by two CART-Cre⁺ RGC subsets onto TC neurons. (A₁) TC neurons receive convergent inputs from CART⁺ RGCs tuned to two opposite directions (model A). (A₂) TC neurons are innervated by CART⁺ RGCs tuned for a specific direction (model B).

(B) Simulated normalized cumulative probability curves based on model A (B₁) or model B (B₂) (STAR Methods).

(C) Comparison of normalized cumulative probability distribution from our experimental (expt) data (BD_{expt}, n = 60 cells; CART_{expt}, n = 74 cells). This dataset includes cells from Figure 4 as well as those acquired in experiments without paired eEPSC measurements. ***p < 0.001, K-S test.

See also Figure S4 and STAR Methods.

motion direction (*BD-CreER*) and two opposite cardinal directions (dorsal and ventral, *Cart-Cre*). Our results showed the following: (1) in the majority of TC neurons recorded, ooDSGC inputs contribute a small portion of total retinal drive, consistent with substantial convergence of ooDSGC inputs with other RGC types; (2) only a small fraction of TC neurons receive primary drive from CART-Cre⁺ or BD-CreER⁺ inputs, as would be expected in a labeled line model; and (3) an analysis of our normalized cumulative probability distributions of CART-Cre⁺ and BD-CreER⁺ inputs suggests that subtypes of ooDSGCs tuned to dorsal and ventral motion tend not to converge onto the same TC neurons.

Convergence of directional information with other retinal inputs

Our findings indicate that most CART-Cre⁺ and BD-CreER⁺ inputs converge with other RGC types. We base our conclusion on the comparisons of absolute amplitudes (Figure 4) and normalized cumulative probability distributions (Figure 5) of ooDSGC-driven oEPSC versus eEPSC from the same cells. Even though the amplitude distributions of CART-Cre⁺ and BD-CreER⁺ inputs are comparable, they are strikingly different from that of input strengths obtained when we activate all convergent inputs onto a TC neuron (Figure 5). This cannot be explained simply by differences in the method of activation or ChR2 expression efficiency. First, the concentration of ChR2 in retinal axons likely reaches levels that reliably trigger action

potential firing by P28, based on our previous experiments comparing oEPSC and eEPSC amplitudes in *Chx10;ChR2* mice (described in Figure S4 of Litvina and Chen⁴¹; see also STAR Methods). Second, as previously published,⁴¹ normalized distributions of both *Chx10;ChR2* oEPSCs (labeling the majority of RGCs with ChR2) and eEPSCs from the same cells yielded similar cumulative probability curves (Figure 5C), despite large differences in the overall amplitude of oEPSCs and eEPSCs attributable to axon severing in slice preparation. This aligned with the basic premise that both oEPSCs and eEPSCs in *Chx10;ChR2* mice drew on the same overall population of inputs. Taken together, these data suggest that the majority of TC neurons receiving on-off directional information are also innervated by other RGC types.^{16,18,19} Our previous study visualizing retinal axon bouton response properties and distribution suggests that these other types may include those tuned to the axis in the same direction or those that differ in their response to luminance (on or off).¹⁹

A small fraction of sampled cells did, however, have a large oEPSC/eEPSC ratio, consistent with a strong ooDSGC drive that can evoke spiking. Less than 15% of responsive TC neurons received primary drive from BD-CreER⁺ or CART-Cre⁺ inputs, despite the axons from both of these RGC subtypes fully covering the recording area. Thus, a small fraction of TC neurons may conduct “labeled line” transmission of ooDSGC information.^{16,18,19} Future studies should investigate the relationship between the tuning properties of the pre- and post-synaptic

neurons in the dLGN and determine the functional relevance of “labeled line” convergence compared with convergent weak, nondominant heterogeneous inputs that persist even in the mature circuit.

Models of convergence of ooDSGCs

We find that ooDSGC inputs mix with other RGC types—but how often do subtypes of ooDSGCs tuned to different directions converge onto the same relay neuron? To better address this question, we tested two simple models of convergence among different subtypes of ooDSGCs. Model A represents one end of a spectrum of connectivity patterns, where CART ooDSGCs of two opposite directions can converge onto the same TC neuron; functionally, this may correspond to a vector sum of their relative weights that contribute to the final direction that the relay neuron is tuned to. On the opposite end of the spectrum, model B proposes that ooDSGC subtypes avoid converging onto the same TC neuron. Several predictions arise from these two models, which we compared with our acquired data.

If we assume that the distribution of peak AMPAR amplitudes of oEPSCs from ooDSGCs tuned to the dorsal direction is similar to that of the ventral (BD) direction, models A and B predict distinct cumulative distributions (Figure 6B). The maximal oEPSC amplitude distribution for CART inputs would be shifted to the right relative to that of BD inputs if all ooDSGCs converge onto a relay neuron (model A). By contrast, if ooDSGCs selective for vertically opposite directions avoid converging together onto the same TC neurons (model B), we would predict that the cumulative histograms would be more similar between CART and BD. Our results show that the cumulative amplitude distribution is similar between CART-Cre⁺ and BD-CreER⁺ RGCs, consistent with the prediction of model B rather than model A. A caveat to these simulations is that they would not detect differences in the cumulative curves if contributions from one ooDSGC subtype are less than 10% of total CART-Cre⁺—this delineates the limitations to our conclusions.

Previous studies have proposed that direction-selective RGCs tuned to opposite directions may converge onto TC neurons to create orientation selectivity.^{19,45,54} Our data and modeling did not identify this as a common convergence pattern for vertically tuned ooDSGCs, as BD-CreER⁺ inputs, representing ventral motion in the retina, tend not to converge with the other CART-Cre⁺ ooDSGCs tuned to dorsal motion. However, this conclusion does not preclude the possibility that opposite direction convergence may occur with relatively low frequency (<10%), as observed with presynaptic calcium imaging¹⁹ or with other direction-selective ganglion cells.

How does the logic of retinal convergence emerge over development? Scenarios include molecular cues, activity-dependent refinement, or mundane sparsity of subtype inputs from the same retinotopic location as might occur toward the periphery of the visual field.¹² The latter scenario would not explain all of our findings, as we record from a region of the dLGN that represents the central and ventral area of the visual space in the azimuth and elevation axes, respectively.⁴⁶ Taken together, our data suggest that whereas RGC inputs tuned to different features of the visual space can converge onto common TC neurons, this mixing does not apply for *subtypes* of ooDSGCs tuned

to opposite directions of motion. Overall, our findings point to a greater complexity in the rules governing convergence of different types versus subtypes of RGCs than previously understood.

STAR★METHODS

Detailed methods are provided in the online version of this paper and include the following:

- **KEY RESOURCES TABLE**
- **RESOURCE AVAILABILITY**
 - Lead contact
 - Materials availability
 - Data and code availability
- **EXPERIMENTAL MODEL AND SUBJECT DETAILS**
 - Animals
- **METHOD DETAILS**
 - Tamoxifen control experiments
 - Two-photon calcium imaging of CART-Cre⁺ RGCs
 - Enucleation
 - Tissue preparation and immunohistochemistry
 - Microscopy
 - Electrophysiology
- **QUANTIFICATION AND STATISTICAL ANALYSIS**
 - Calcium imaging analysis
 - Axonal distribution analysis
 - Simulation of ooDSGCs innervation
 - Rationale for oEPSC/eEPSC classification
 - Data analysis and statistics

SUPPLEMENTAL INFORMATION

Supplemental information can be found online at <https://doi.org/10.1016/j.cub.2022.06.023>.

ACKNOWLEDGMENTS

We thank Drs. M. Andermann, M. Do, L. Liang, and J. Reggiani and all other members of the Chen lab for helpful discussions about the project and manuscript and S. Barry for technical assistance. We thank Dr. Hongkui Zeng from the Allen Institute for providing the *Cart-IRES-cre-D* mouse line and Dr. Zhigang He for the RBPMS antibody. Support was provided by the NIH RO1EY013613 to C.C., T32 NS007473 to T.S., the Edward R. and Anne G. Lefler Foundation Predoctoral Fellowship to E.Y.L., and NIH RO1 NS109990 to W.W. We thank the IDDRC Cellular Imaging Core, funded in part by S10OD016453 and U54 HD090255, for access to their shared confocal microscopes.

AUTHOR CONTRIBUTIONS

Q.J., E.Y.L., and C.C. designed the experiments and wrote the paper. W.W. and H.A.L. designed the retinal imaging experiments and summarized the description and results of these experiments in the manuscript. H.A.L. conducted calcium imaging experiments for the retinas of *Cart;GcaMP6f* mice. G.S. performed the immunostaining of mouse retinas and dLGN slices. Q.J. and E.Y.L. conducted the whole-cell patch recordings from dLGN neurons. T.S. did the enucleation surgeries and collected the samples. This work was conducted while E.Y.L. was employed at Boston Children’s Hospital. E.Y.L. edited parts of the manuscript while employed by NINDS. The opinions expressed in this article are the authors’ own and do not reflect the view of the National Institutes of Health, the Department of Health and Human Services, or the United States government.

DECLARATION OF INTERESTS

The authors declare no competing interests.

Received: May 16, 2021

Revised: April 22, 2022

Accepted: June 9, 2022

Published: July 5, 2022

REFERENCES

- Baden, T., Euler, T., and Berens, P. (2020). Understanding the retinal basis of vision across species. *Nat. Rev. Neurosci.* *21*, 5–20.
- Martersteck, E.M., Hirokawa, K.E., Everts, M., Bernard, A., Duan, X., Li, Y., Ng, L., Oh, S.W., Ouellette, B., Royall, J.J., et al. (2017). Diverse central projection patterns of retinal ganglion cells. *Cell Rep.* *18*, 2058–2072.
- Baden, T., Berens, P., Franke, K., Román Rosón, M.R., Bethge, M., and Euler, T. (2016). The functional diversity of retinal ganglion cells in the mouse. *Nature* *529*, 345–350.
- Sanes, J.R., and Masland, R.H. (2015). The types of retinal ganglion cells: current status and implications for neuronal classification. *Annu. Rev. Neurosci.* *38*, 221–246.
- Bae, J.A., Mu, S., Kim, J.S., Turner, N.L., Tartavull, I., Kemnitz, N., Jordan, C.S., Norton, A.D., Silversmith, W.M., and Prentki, R. (2018). Digital museum of retinal ganglion cells with dense anatomy and physiology. *Cell* *173*, 1293–1306. e19.
- Rheume, B.A., Jereen, A., Bolisetty, M., Sajid, M.S., Yang, Y., Renna, K., Sun, L., Robson, P., and Trakhtenberg, E.F. (2018). Single cell transcriptome profiling of retinal ganglion cells identifies cellular subtypes. *Nat. Commun.* *9*, 2759.
- Tran, N.M., Shekhar, K., Whitney, I.E., Jacobi, A., Benhar, I., Hong, G., Yan, W., Adiconis, X., Arnold, M.E., and Lee, J.M. (2019). Single-cell profiles of retinal ganglion cells differing in resilience to injury reveal neuroprotective genes. *Neuron* *104*, 1039–1055. e12.
- Kay, J.N., De la Huerta, I., Kim, I.-J., Zhang, Y., Yamagata, M., Chu, M.W., Meister, M., and Sanes, J.R. (2011). Retinal ganglion cells with distinct directional preferences differ in molecular identity, structure, and central projections. *J. Neurosci.* *31*, 7753–7762.
- Vaney, D.J., Sivyer, B., and Taylor, W.R. (2012). Direction selectivity in the retina: symmetry and asymmetry in structure and function. *Nat. Rev. Neurosci.* *13*, 194–208.
- Barlow, H.B., and Hill, R.M. (1963). Selective sensitivity to direction of movement in ganglion cells of the rabbit retina. *Science* *139*, 412–414.
- Borst, A., and Euler, T. (2011). Seeing things in motion: models, circuits, and mechanisms. *Neuron* *71*, 974–994.
- Sabbah, S., Gemmer, J.A., Bhatia-Lin, A., Manoff, G., Castro, G., Siegel, J.K., Jeffery, N., and Berson, D.M. (2017). A retinal code for motion along the gravitational and body axes. *Nature* *546*, 492–497.
- Dhande, O.S., Stafford, B.K., Lim, J.-H.A., and Huberman, A.D. (2015). Contributions of retinal ganglion cells to subcortical visual processing and behaviors. *Annu. Rev. Vision Sci.* *1*, 291–328.
- Glees, P., and le Gros Clark, W.E. (1941). The termination of optic fibres in the lateral geniculate body of the monkey. *J. Anat.* *75*, 295–308.3.
- Sherman, S.M., and Guillery, R.W. (1996). Functional organization of thalamocortical relays. *J. Neurophysiol.* *76*, 1367–1395.
- Rompani, S.B., Müllner, F.E., Wanner, A., Zhang, C., Roth, C.N., Yonehara, K., and Roska, B.J.N. (2017). Different modes of visual integration in the lateral geniculate nucleus revealed by single-cell-initiated trans-synaptic tracing. *Neuron* *93*, 767–776. e6.
- Morgan, J.L., Berger, D.R., Wetzell, A.W., and Lichtman, J.W. (2016). The fuzzy logic of network connectivity in mouse visual thalamus. *Cell* *165*, 192–206.
- Rosón, M.R., Bauer, Y., Kotkat, A.H., Berens, P., Euler, T., and Busse, L. (2019). Mouse dLGN receives functional input from a diverse population of retinal ganglion cells with limited convergence. *Neuron* *102*, 462–476. e8.
- Liang, L., Fratzl, A., Goldey, G., Ramesh, R.N., Sugden, A.U., Morgan, J.L., Chen, C., and Andermann, M.L. (2018). A fine-scale functional logic to convergence from retina to thalamus. *Cell* *173*, 1343–1355. e24.
- Rogge, G., Jones, D., Hubert, G.W., Lin, Y., and Kuhar, M.J. (2008). CART peptides: regulators of body weight, reward and other functions. *Nat. Rev. Neurosci.* *9*, 747–758.
- Kim, I.J., Zhang, Y., Meister, M., and Sanes, J.R. (2010). Laminar restriction of retinal ganglion cell dendrites and axons: subtype-specific developmental patterns revealed with transgenic markers. *J. Neurosci.* *30*, 1452–1462.
- Jo, A., Xu, J., Deniz, S., Cherian, S., DeVries, S.H., and Zhu, Y. (2018). Intersectional strategies for targeting amacrine and ganglion cell types in the mouse retina. *Front. Neural Circuits* *12*, 66.
- Land, P.W., Kyonka, E., and Shamalla-Hannah, L. (2004). Vesicular glutamate transporters in the lateral geniculate nucleus: expression of VGLUT2 by retinal terminals. *Brain Res* *996*, 251–254.
- Lein, E.S., Hawrylycz, M.J., Ao, N., Ayres, M., Bensinger, A., Bernard, A., Boe, A.F., Boguski, M.S., Brockway, K.S., Byrnes, E.J., et al. (2007). Genome-wide atlas of gene expression in the adult mouse brain. *Nature* *445*, 168–176.
- Bakker, R., Tiesinga, P., and Kötter, R. (2015). The scalable brain atlas: instant web-based access to public brain atlases and related content. *Neuroinformatics* *13*, 353–366.
- Huberman, A.D., Wei, W., Elstrott, J., Stafford, B.K., Feller, M.B., and Barres, B.A. (2009). Genetic identification of an On-Off direction-selective retinal ganglion cell subtype reveals a layer-specific subcortical map of posterior motion. *Neuron* *62*, 327–334.
- Rivlin-Etzion, M., Zhou, K., Wei, W., Elstrott, J., Nguyen, P.L., Barres, B.A., Huberman, A.D., and Feller, M.B. (2011). Transgenic mice reveal unexpected diversity of on-off direction-selective retinal ganglion cell subtypes and brain structures involved in motion processing. *J. Neurosci.* *31*, 8760–8769.
- Cruz-Martin, A., El-Danaf, R.N., Osakada, F., Sriram, B., Dhande, O.S., Nguyen, P.L., Callaway, E.M., Ghosh, A., and Huberman, A.D. (2014). A dedicated circuit links direction-selective retinal ganglion cells to the primary visual cortex. *Nature* *507*, 358–361.
- Bickford, M.E., Zhou, N., Krahe, T.E., Govindaiah, G., and Guido, W. (2015). Retinal and tectal “driver-like” inputs converge in the shell of the mouse dorsal lateral geniculate nucleus. *J. Neurosci.* *35*, 10523–10534.
- Bickford, M.E., Slusarczyk, A., Dilger, E.K., Krahe, T.E., Kucuk, C., and Guido, W. (2010). Synaptic development of the mouse dorsal lateral geniculate nucleus. *J. Comp. Neurol.* *518*, 622–635.
- Hong, Y.K., Park, S., Litvina, E.Y., Morales, J., Sanes, J.R., and Chen, C. (2014). Refinement of the retinogeniculate synapse by bouton clustering. *Neuron* *84*, 332–339.
- Rafols, J.A., and Valverde, F. (1973). The structure of the dorsal lateral geniculate nucleus in the mouse. A Golgi and electron microscopic study. *J. Comp. Neurol.* *150*, 303–332.
- Robson, J.A., and Mason, C.A. (1979). The synaptic organization of terminals traced from individual labeled retino-geniculate axons in the cat. *Neuroscience* *4*, 99–111.
- Wilson, J., Bose, N., and Sherman, S. (1984). Fine structural morphology of identified X- and Y-cells in the cat’s lateral geniculate nucleus. *Proc. R. Soc. Lond. B* *221*, 411–436.
- Hamos, J.E., Van Horn, S.C., Raczkowski, D., and Sherman, S.M. (1987). Synaptic circuits involving an individual retinogeniculate axon in the cat. *J. Comp. Neurol.* *259*, 165–192.
- Hooks, B.M., and Chen, C. (2006). Distinct roles for spontaneous and visual activity in remodeling of the retinogeniculate synapse. *Neuron* *52*, 281–291.
- Hong, Y.K., Burr, E.F., Sanes, J.R., and Chen, C. (2019). Heterogeneity of retinogeniculate axon arbors. *Eur. J. Neurosci.* *49*, 948–956.

38. Turner, J.P., and Salt, T.E. (1998). Characterization of sensory and corticothalamic excitatory inputs to rat thalamocortical neurones in vitro. *J. Physiol.* *510*, 829–843.
39. Chen, C., and Regehr, W.G. (2000). Developmental remodeling of the retinogeniculate synapse. *Neuron* *28*, 955–966.
40. Chen, C., and Regehr, W.G. (2003). Presynaptic modulation of the retinogeniculate synapse. *J. Neurosci.* *23*, 3130–3135.
41. Litvina, E.Y., and Chen, C. (2017). Functional convergence at the retinogeniculate synapse. *Neuron* *96*, 330–338. e5.
42. Hammer, S., Monavarfeshani, A., Lemon, T., Su, J., and Fox, M.A. (2015). Multiple retinal axons converge onto relay cells in the adult mouse thalamus. *Cell Rep* *12*, 1575–1583.
43. Liu, X., and Chen, C. (2008). Different roles for AMPA and NMDA receptors in transmission at the immature retinogeniculate synapse. *J. Neurophysiol.* *99*, 629–643.
44. Reese, B. (1988). Hidden lamination in the dorsal lateral geniculate nucleus: the functional organization of this thalamic region in the rat. *Brain Res. Rev.* *13*, 119–137.
45. Marshel, J.H., Kaye, A.P., Nauhaus, I., and Callaway, E.M. (2012). Anterior-posterior direction opponency in the superficial mouse lateral geniculate nucleus. *Neuron* *76*, 713–720.
46. Piscopo, D.M., El-Danaf, R.N., Huberman, A.D., and Niell, C.M. (2013). Diverse visual features encoded in mouse lateral geniculate nucleus. *J. Neurosci.* *33*, 4642–4656.
47. Scholl, B., Tan, A.Y., Corey, J., and Priebe, N.J. (2013). Emergence of orientation selectivity in the mammalian visual pathway. *J. Neurosci.* *33*, 10616–10624.
48. Zhao, X., Chen, H., Liu, X., and Cang, J. (2013). Orientation-selective responses in the mouse lateral geniculate nucleus. *J. Neurosci.* *33*, 12751–12763.
49. Sun, W., Tan, Z., Mensh, B.D., and Ji, N. (2016). Thalamus provides layer 4 of primary visual cortex with orientation- and direction-tuned inputs. *Nat. Neurosci.* *19*, 308–315.
50. Kondo, S., and Ohki, K. (2016). Laminal differences in the orientation selectivity of geniculate afferents in mouse primary visual cortex. *Nat. Neurosci.* *19*, 316–319.
51. Rasmussen, R., Matsumoto, A., Sietam, M.D., and Yonehara, K. (2020). A segregated cortical stream for retinal direction selectivity. *Nat. Commun.* *11*, 1.
52. Hillier, D., Fiscella, M., Drinnenberg, A., Trenholm, S., Rompani, S.B., Raics, Z., Katona, G., Juettner, J., Hierlemann, A., Rozsa, B., et al. (2017). Causal evidence for retina-dependent and-independent visual motion computations in mouse cortex. *Nat. Neurosci.* *20*, 960–968.
53. Shi, X., Barchini, J., Ledesma, H.A., Koren, D., Jin, Y., Liu, X., Wei, W., and Cang, J. (2017). Retinal origin of direction selectivity in the superior colliculus. *Nat. Neurosci.* *20*, 550–558.
54. Stafford, B.K., and Huberman, A.D. (2017). Signal integration in thalamus: labeled lines go cross-eyed and blurry. *Neuron* *93*, 717–720.
55. Rodriguez, A.R., de Sevilla Müller, L.P., and Brecha, N.C. (2014). The RNA binding protein RBPMS is a selective marker of ganglion cells in the mammalian retina. *J. Comp. Neurol.* *522*, 1411–1443.
56. Norsworthy, M.W., Bei, F., Kawaguchi, R., Wang, Q., Tran, N.M., Li, Y., Brommer, B., Zhang, Y., Wang, C., and Sanes, J.R. (2017). Sox11 expression promotes regeneration of some retinal ganglion cell types but kills others. *Neuron* *94*, 1112–1120. e4.
57. Rowan, S., and Cepko, C.L. (2004). Genetic analysis of the homeodomain transcription factor Chx10 in the retina using a novel multifunctional BAC transgenic mouse reporter. *Dev. Biol.* *271*, 388–402.
58. Madisen, L., Mao, T., Koch, H., Zhuo, J.-M., Berenyi, A., Fujisawa, S., Hsu, Y.-W., Garcia, A.J., III, Gu, X., Zanella, S., et al. (2012). A toolbox of Cre-dependent optogenetic transgenic mice for light-induced activation and silencing. *Nat. Neurosci.* *15*, 793–802.
59. Wei, W., Elstrott, J., and Feller, M.B. (2010). Two-photon targeted recording of GFP-expressing neurons for light responses and live-cell imaging in the mouse retina. *Nat. Protoc.* *5*, 1347–1352.
60. Brainard, D.H., and Vision, S. (1997). The psychophysics toolbox. *Spat. Vision* *10*, 433–436.
61. Pressler, R.T., and Regehr, W.G. (2013). Metabotropic glutamate receptors drive global persistent inhibition in the visual thalamus. *J. Neurosci.* *33*, 2494–2506.
62. Hauser, J.L., Liu, X., Litvina, E.Y., and Chen, C. (2014). Prolonged synaptic currents increase relay neuron firing at the developing retinogeniculate synapse. *J. Neurophysiol.* *112*, 1714–1728.
63. Yang, Y.C., Hu, C.C., Huang, C.S., and Chou, P.Y. (2014). Thalamic synaptic transmission of sensory information modulated by synergistic interaction of adenosine and serotonin. *J. Neurochem.* *128*, 852–863.
64. Kingston, A.E., Ornstein, P.L., Wright, R.A., Johnson, B.G., Mayne, N.G., Burnett, J.P., Belagaje, R., Wu, S., and Schoepp, D.D. (1998). LY341495 is a nanomolar potent and selective antagonist of group II metabotropic glutamate receptors. *Neuropharmacology* *37*, 1–12.
65. Hauser, J.L., Edson, E.B., Hooks, B.M., and Chen, C. (2013). Metabotropic glutamate receptors and glutamate transporters shape transmission at the developing retinogeniculate synapse. *J. Neurophysiol.* *109*, 113–123.
66. Bos, R., Gainer, C., and Feller, M.B. (2016). Role for visual experience in the development of direction-selective circuits. *Curr. Biol.* *26*, 1367–1375.
67. Tiriác, A., Bistrong, K., Pitcher, M.N., Tworj, J.M., and Feller, M.B. (2022). The influence of spontaneous and visual activity on the development of direction selectivity maps in mouse retina. *Cell Rep.* *38*, 110225.

STAR★METHODS

KEY RESOURCES TABLE

REAGENT or RESOURCE	SOURCE	IDENTIFIER
Antibodies		
Chicken anti-GFP	AVES Labs	Cat# GFP-1020; RRID: AB_10000240
Rabbit anti-CART	Phoenix Pharmaceuticals	Cat# H-003-62; RRID: AB_2313614
Guinea pig anti-RBPMS	Zhigang He's Lab ^{55,56}	N/A
Goat anti-chicken IgY (H+L) (Alexa Fluor 488)	Invitrogen	Cat# A11039; RRID: AB_2534096
Goat anti-rabbit IgG (H+L) (Alexa Fluor Plus 555)	Invitrogen	Cat# A32732; RRID: AB_2633281
Goat anti-guinea pig IgG H&L (Alexa Fluor 405)	Abcam	Cat# ab175678; RRID: AB_2827755
Rabbit anti-GFP	Abcam	Cat# ab290; RRID: AB_303395
Guinea pig polyclonal anti-VGluT2	Millipore	Cat# AB2251-I; RRID: AB_2665454
Goat anti-rabbit IgG (H+L) (Alexa Fluor Plus 488)	Invitrogen	Cat# A32731; RRID: AB_2633280
Goat anti-guinea pig IgG (H+L) (Alexa Fluor Plus 555)	Invitrogen	Cat# A21435; RRID: AB_2535856
Chemicals, peptides, and recombinant proteins		
(+)-Bicuculline	Tocris	Cat# 0130
CGP 55845 hydrochloride	Tocris	Cat# 1248
DPCPX	Tocris	Cat# 0439
LY341495	Tocris	Cat# 1209
Tamoxifen	Sigma	Cat# 85256
Deposited data		
Schematics in Figure 2	Scalable Brain Atlas ^{24,25}	https://scalablebrainatlas.incf.org/composer/?template=ABA_v3
Code for simulations in Figures 6 and S4	This paper	https://github.com/CClabmembers/2022_CurrentBiology.git
Experimental models: Organisms/strains		
Mouse: Cart-IRES2-Cre-D	Hongkui Lab, Allen Brain Institute, ^{2,21} now available in the Jackson Laboratory	Cat# 028533; RRID: IMSR_JAX:028533
Mouse: Ai95D	The Jackson Laboratory	Cat# 028865; RRID: IMSR_JAX:028865
Mouse: BD-CreER	Joshua Sanes's Lab ²¹	N/A
Mouse: Chx10-Cre	The Jackson Laboratory ⁵⁷	Cat# 005105; RRID: IMSR_JAX:005105
Mouse: Ai32	The Jackson Laboratory	Cat#012569; RRID: IMSR_JAX:012569
Software and algorithms		
MATLAB_R2019b	Mathworks	https://www.mathworks.com/products/matlab.html ; RRID: SCR_001622
ImageJ (Fiji)	NIH – public domain	https://imagej.net/Fiji ; RRID: SCR_002285
Igor Pro	WaveMetrics	https://www.wavemetrics.com/products/igorpro ; RRID: SCR_000325
Prism 8	Graphpad	https://www.graphpad.com/scientific-software/prism/ ; RRID: SCR_005375
JMP	SAS Institute	http://www.jmp.com/en_us/software/jmp.html ; RRID: SCR_014242

RESOURCE AVAILABILITY

Lead contact

Further information and requests for resources and reagents should be directed to and will be fulfilled by the lead contact, Chinfai Chen (Chinfai.Chen@childrens.harvard.edu).

Materials availability

This study did not generate new unique reagents.

Data and code availability

The published article includes all data generated or analyzed during this study. Relevant codes for simulation analysis are available at: (https://github.com/CClabmembers/2022_CurrentBiology.git). Any additional information required to reanalyze the data reported in this paper is available from the [lead contact](#) upon request.

EXPERIMENTAL MODEL AND SUBJECT DETAILS

Animals

All animal procedures were in compliance with the NIH Guide for the Care and Use of Laboratory Animals and approved by the Institutional Animal and Care and Use Committee (IACUC) at Boston Children's Hospital. To detect the specificity of ooDSGC labeling in *Cart-IRES2-Cre-D* mice (obtained from Hongkui Zeng Lab, Allen Brain Institute),^{2,21} they were crossed with *Ai95D* floxed GCaMP6f mice (Jackson Laboratory). Mice of ages P19-P33 of either sex were used. To drive the expression of ChR2 expression in RGCs, *Cart-IRES2-Cre-D*, *BD-CreER* (obtained from Joshua Sanes Lab),²¹ and *Chx10-Cre* mice (JAX 005105)⁵⁷ were crossed with fluorescently-tagged Cre-dependent ChR2-EYFP expressing mice (homozygous *Ai32* mice, JAX 012569),⁵⁸ respectively, yielding progeny expressing ChR2 and EYFP in the retina. We refer to the resulting crosses as "*Cart;ChR2*", "*BD;ChR2*", and "*Chx10;ChR2*", respectively. Tamoxifen (200 μ g, Sigma) was intraperitoneally injected at P0 or P1 to *BD;ChR2* mice for labeling of BD⁺ RGCs, or to *Chx10;ChR2* mice to elaborate the effect of tamoxifen on functional synaptic connectivity. Data from *BD;ChR2* mice with fewer than 200 EYFP⁺ RGCs were excluded from analysis (Figure S2A). Male and female animals aged P27-34 were employed.

METHOD DETAILS

Tamoxifen control experiments

Since expression of ChR2 in *BD;ChR2* mice was dependent on binding of the estrogen receptor, we asked whether the presence of tamoxifen may disrupt maturation of retinogeniculate synapses. We injected tamoxifen into *Chx10;ChR2* mice, which label all RGCs,⁴¹ with the same dosing as our experiments with *BD;ChR2* mice. Both oEPSCs and electrically stimulated EPSCs (eEPSCs) exhibited similar average amplitude in tamoxifen-injected mice when compared to those without the drug injection (Figure S3B). These results alleviate concerns of deleterious effects of tamoxifen on retinogeniculate connectivity.

Two-photon calcium imaging of CART-Cre⁺ RGCs

Whole-mount retina preparation

After dark adaptation for > 30 mins, mice were anesthetized with isoflurane and euthanized by decapitation. Retinas were isolated from the pigment epithelium under infrared illumination at room temperature in oxygenated Ames' medium (Sigma-Aldrich, St. Louis, MO). Retinas were cut into dorsal and ventral halves using scleral marks as identified in Wei et al.⁵⁹ and mounted on top of a 3-4 mm² hole in a small piece of filter paper with ganglion-cell-layer-up on top (Millipore, Billerica, MA). The mounted retinas were kept in darkness at room temperature in Ames' medium bubbled with 95% O₂/5% CO₂ until use (0-8 hr).

Visual stimulation

A white organic light-emitting display (OLEDXL, eMagin, Bellevue, WA; 800 × 600 pixel resolution, 60 Hz refresh rate) was controlled by an Intel Core Duo computer with a Windows 7 operating system and was presented to the retina at a resolution of 1.1 μ m/pixel. Moving bar stimuli were generated by MATLAB and the Psychophysics Toolbox,⁶⁰ and projected through the condenser lens of the two-photon microscope onto the photoreceptor layer. For the moving bar stimulus, a positive-contrast bar (275 μ m wide, 660 μ m long) moved along the long axis in 8 pseudo-randomly chosen directions at a speed of 550 μ m/sec over a 660 μ m-diameter field on the retina; and four trials were recorded for each direction.

Calcium imaging of GCaMP6f fluorescence

GCaMP6f fluorescence of isolated retinas in oxygenated Ames at 32-33°C was imaged in a customized two-photon laser scanning fluorescence microscope (Bruker Nano Surfaces Division). GCaMP6f was excited by a Ti:sapphire laser (Coherent, Chameleon Ultra II, Santa Clara, CA) tuned to 920 nm, and the laser power was adjusted to avoid saturation of the fluorescent signal. Onset of laser scanning induces a transient two-photon response that adapts to the baseline in \sim 3 s. Therefore, to ensure the complete adaptation of this laser-induced response and a stable baseline, visual stimuli were given after 20 s of continuous laser scanning. To separate the visual stimulus from GCaMP6f fluorescence, a band-pass filter (Semrock, Rochester, MA) was placed on the OLED to pass blue light

peaked at 470 nm, while two notched filters (Bruker Nano Surfaces Division) were placed before the photomultiplier tubes to block light of the same wavelength. The objective was a water immersion objective (20x, Olympus). Time series of each imaging window were collected at 17 Hz or higher.

Enucleation

To detect whether there are other sources of CART-Cre⁺ or BD-CreER⁺ inputs in the dLGN of *Cart-IREG2-Cre-D* and *BD-CreER* mice apart from the retina, *Cart;ChR2* and *BD;ChR2* mice were enucleated from both eyes at P20–24, and sacrificed after 8 days of enucleation. The distribution of GFP labeling in the dLGN was then analyzed and compared to control animals housed in normal light-dark cycle area and with both eyes present.

Tissue preparation and immunohistochemistry

Mice were anesthetized with 50mg/kg pentobarbital and transcardially perfused with 0.1M phosphate buffered saline (PBS) immediately followed by 4% w/v paraformaldehyde (PFA) in PBS. Retinas were dissected and post-fixed in 4% PFA for 30 min, and restored in PBS before immunostaining. Brains were post-fixed overnight in 4% PFA at 4°C and rinsed in PBS. Brain slices containing dLGN were coronally sectioned through Leica VT1000 vibratome with thickness of 60 μm. Following *in vitro* electrophysiology experiments, retinas and parasagittally sectioned brain slices (250 μm) were also collected, incubated in 4% PFA for 20 min, and stored in PBS until immunostaining, to confirm the density and specificity of labeling after each experiment.

In whole-mount retinas, we identified RGCs by the expression of RBPMS,⁵⁵ and immunostained for CART and GFP (Figures 1C₁ and D₁). For retinal staining, dissected whole mount retinas were blocked in PBS containing 5% normal goat serum (NGS) and 0.1% Triton X-100 at room temperature for 1 hr. Then primary antibodies were applied in PBS containing 0.5% Triton and 2% NGS: chicken anti-GFP (1:1000; GFP-1020, AVES Labs), rabbit anti-CART (1:2000; H-003-62, Phoenix Pharmaceuticals), guinea pig anti-RBPMS (1:1000; a gift from Zhigang He's lab⁵⁶) at 4°C for 2–3 days. After rinsing with 0.1% Triton/PBS, retinas were incubated with secondary antibodies at 4°C for another 2–3 days: goat anti-chicken antibody conjugated to Alexa Fluor 488 (1:1000; A11039, Invitrogen), goat anti-rabbit 555 (1:1000; A32732, Invitrogen), and goat anti-guinea pig 405 (1:1000; ab175678, Abcam). Retinas were then mounted and cover-slipped with Vectashield (VectorLabs H-1000).

Brain slices containing dLGN were stained with GFP and vesicular glutamate transporter (VGluT2) by incubating with rabbit anti-GFP (1:2000; ab290, Abcam) and guinea pig polyclonal anti-VGluT2 (1:2000; ab2251-I, Millipore), followed by secondary antibody incubation with goat anti-rabbit 488 (1:1000; a32731, Invitrogen) and goat anti-guinea pig 555 (1:1000; a21435, Invitrogen).

Microscopy

To measure the specificity of marker expression in CART-Cre⁺ or BD-CreER⁺ RGCs, images of the retina (12 fields of view taken from 3 *Cart;ChR2* or *BD;ChR2* mice each) were acquired with Zeiss LSM 700 using a 20x objective to detect the signals of GFP, CART, and RBPMS. Quantification was performed manually using ImageJ. To check the reliability of ChR2 expression in *Cart;ChR2* and *BD;ChR2* mice used for *in vitro* electrophysiology studies, retinas from these animals were collected, flat-mounted, and tile-imaged on the Nikon 80i epifluorescent scope using 10x or 20x objective. The images were then reassembled in Photoshop (Adobe), and the number of GFP⁺ RGCs was quantified manually using ImageJ. To assess the colocalization of GFP and VGluT2 in the dLGN, brain slices containing dLGN were imaged with Zeiss LSM 700 or 710 confocal microscopes (Zeiss, Olympus) equipped with 5x–60x objectives and Leica TCS SP8 Laser Scanning Confocal (STED One) with 100x objective. Z-stack and tiling were automated with built-in functions in Zeiss imaging software on the LSM 710.

Electrophysiology

Brain slices containing the optic tracts (OTs) and dLGN were prepared as previously described.⁴¹ Briefly, mice were anesthetized using isoflurane and decapitated into oxygenated (95% O₂/5% CO₂) ice-cold cutting solution (in mM): 130 K-gluconate, 15 KCl, 0.05 EGTA, 20 HEPES, and 25 glucose (pH 7.4 adjusted with NaOH, 310–315 mOsm).⁶¹ The brain was then removed quickly and immersed in the ice-cold cutting solution for 60 seconds. To obtain slices maintaining continuity of retinogeniculate fiber inputs, parasagittal sectioning was conducted as previously described.³⁸ The brain was cut with a steel razor blade, then sectioned into 250 μm-thick slices in the oxygenated ice-cold cutting solution using a sapphire blade (Delaware Diamond Knives, Wilmington, DE) on a vibratome (VT1200S; Leica, Deerfield, IL). The slices containing dLGN and OTs were allowed to recover at 30°C for 20 minutes in oxygenated saline solution (in mM): 125 NaCl, 26 NaHCO₃, 1.25 NaH₂PO₄, 2.5 KCl, 1.0 MgCl₂, 2.0 CaCl₂, and 25 glucose (pH 7.4, 310–315 mOsm).

Whole-cell patch clamp was conducted on TC neurons located in the ventral posterior region of the dLGN under room temperature (lateral or middle section in Figure 2B). Cells were visualized through a monitor with projection from the camera of a DIC-equipped microscope (Olympus). Glass pipettes (Drummond Scientific) were pulled on Sutter p87 Flaming/Brown micropipette puller (Sutter Instruments), and filled with internal solution containing (in mM): 35 CsF, 100 CsCl, 10 EGTA, 10 HEPES, and L-type calcium channel antagonist 0.1 methoxyverapamil (pH 7.3, 290–300 mOsm) to optimize the pipette resistance to be 1.5–2.0 MOhm. Patch recordings were performed using a MultiClamp 700B (Axon Instruments, Foster City, CA), filtered at 1kHz, and digitized at 4–50 kHz with an ITC-18 interface (Instrutech). To detect potential differences in the maturation of the synaptic inputs, both AMPA and NMDA receptor (AMPA and NMDAR)-mediated currents were obtained by holding the membrane potential of recorded cells at -70 and +40 mV (Figure 3A right), respectively, since the ratio of these currents can provide information on the degree of maturation of the synapse.³⁶

Intertrial intervals were kept at 30 seconds. Since NMDAR currents are easily saturated, only AMPAR oEPSCs were analyzed for the following study. Access resistance was monitored throughout the experiment and evaluated in offline analysis. Experiments with access resistance changing over 20% were removed from analysis. To isolate excitatory synaptic currents, cells were recorded at room temperature in oxygenated saline solution containing 20 μM of bicuculline (GABA_AR antagonist), 2 μM of CGP55845 (GABA_BR blocker), 10 μM of DPCPX (antagonist of A1 adenosine receptors), and 50 μM of LY341495 (blocker of presynaptic group II mGluRs),^{39,62–65} to block inhibitory circuits and neurotransmitter receptors that modulate retinogeniculate transmission.^{39,40}

To obtain ChR2-evoked EPSC (referred to as “oEPSC”), recorded slices received a single pulse of full-field illumination of blue light through a water immersion 60x objective (Olympus LUMplanFL N 60x/1.00W), which was set at the distance where the cells and labeled axons could be visualized clearly. The blue light (470 nm, 83 mW/mm²) was supplied by a CoolLED pE unit, lasting for 0.2 msec at highest power (100%, 83 mW/mm²) to obtain maximal oEPSC. To assess whether the post-synaptic responses can be saturated under the highest power, responses evoked by different light power were normalized to the maximal amplitude from each animal and averaged and then plotted as a function of light intensity (Figure S3A, left).

To obtain electrical stimulated EPSC (referred to as “eEPSC”), a pair of electrodes were filled with saline solution, and lowered onto the slices. One of the electrodes was inserted into the OTs to electrically stimulate the retinogeniculate inputs. The other electrode was immersed in the bath but did not touch the brain slice, serving as the ground. Electrical stimuli were supplied by a stimulus isolator (WPI A365) delivering a 0.2 msec pulse with 200 μA for maximal eEPSC. Maximal eEPSC amplitude was determined from the average of 3–5 trials. All eEPSCs reached a saturating response when $\geq 200 \mu\text{A}$ of electrical stimulation was applied (Figure S3A, right).

QUANTIFICATION AND STATISTICAL ANALYSIS

Calcium imaging analysis

Analysis was performed using ImageJ and MATLAB. Raw frames were uploaded onto ImageJ software in which regions of interest (ROIs) were manually drawn to enclose the soma of each GCaMP6f expressing cell and for a background region where there was no detectable GCaMP6f expression. These manually selected ROIs were then imported into MATLAB, where custom written scripts were used to calculate the average intensity over time for all ROIs. In MATLAB, the background trace was subtracted from the light responsive somatic traces to remove noise. Background subtracted traces were smoothed using an averaging sliding window of 3 datapoints (approximately 90–150 ms depending on framerate). We then fitted the baseline fluorescence over time to single or two-term exponential decay function using datapoints corresponding to the time between each moving bar sweep (4 seconds). Using the fitted F_0 traces, raw fluorescence data was transformed to $\Delta F/F_0 = (F - F_0)/F_0$. Traces were then resampled to 75 Hz through boxcar method and smoothed using an average sliding window of 5 data points (~ 67 ms). $\Delta F/F_0$ traces were then clipped, sorted by visual stimulus direction, and averaged over the 4 trials.

Prior to further analysis, traces were subjected to a response quality test $QI = \text{Var}(\langle \text{Trial} \rangle_1^4)_{\text{time}} / (\text{Var}(\text{Trial})_{\text{time}})_1^4$ to ensure consistency across trials.³ If all trials are identical such that the mean response is a perfect representative of the response, QI is equal to 1. On the other hand, if all trials are completely random with fixed variance (so that the mean response is not informative about the individual trial responses), QI falls towards $(1 / \text{num. trials})$. We implemented a quality threshold of QI 0.40 for the response from a given cell to be considered for further analysis.

The 660 μm long bar allows for clear separation between responses to the leading and trailing edge of the moving bar. Cells showing responses to the leading edge were classified as ON, cells showing responses to the trailing edge were classified as OFF, and cells showing responses to both leading and trailing edges were classified as ON-OFF. Tuning curves were plotted using the average $\Delta F/F_0$ for each direction.

For each cell, we calculated DSI = $(R_{\text{Pref}} - R_{\text{Null}}) / (R_{\text{Pref}} + R_{\text{Null}})$, where R_{Pref} is the cell’s response at the preferred direction (i.e., maximal response), and R_{Null} is the cell’s response to the direction opposite to the preferred one. Cells with DSI ≥ 0.4 were identified as direction selective. Additionally, gDSI or vector sum was calculated as $gDSI = \sum R_{\theta} e^{i\theta} / \sum R_{\theta}$ and the preferred direction was determined as the angle of the vector sum $\varphi = \arg(\sum R_{\theta} e^{i\theta})$. Similarly, orientation selectivity was tested using OSI = $(\sum R_{\text{Pref}} - \sum R_{\text{Null}}) / (\sum R_{\text{Pref}} + \sum R_{\text{Null}})$, where R_{Pref} and R_{Null} correspond to responses along the preferred and null axes. gOSI was calculated as $gOSI = \sum R_{\theta} e^{2i\theta} / \sum R_{\theta}$. Cells with OSI ≥ 0.4 were identified as orientation selective. Cells with DSI < 0.4 and OSI < 0.4 were classified as broadly tuned. Lastly, cells with negative-going $\Delta F/F_0$ responses during the duration of the moving bar stimulus were identified as suppressed-by-contrast.

To determine which subtypes of ooDSGCs (nasal-, temporal-, ventral-, and/or dorsal-preferring) are represented in the *Cart-IRES2-Cre-D* mouse line, we used a similar clustering algorithm described in previous studies.^{66,67} In short, K-means clustering was used to group the preferred directions of identified ooDSGCs (by criteria described above) into predetermined number of clusters ($n = 2$ –6 clusters). This technique assigns each datapoint to a given based on the nearest centroid, or mean value of a cluster. Then, the fitness of the number of clusters was determined by silhouette value (SV) analysis:

$$SV(i) = \frac{(b(i) - a(i))}{\max(a(i), b(i))}$$

where $a(i)$ is the average angular distance between datapoint i and all other datapoints in the same cluster and $b(i)$ is the average angular distance between datapoint i and all other datapoints in the nearest cluster. The SV values for all datapoint were averaged for all conditions (k-means clustering with $n = 2-6$ clusters). An average SV value approaching 1 suggests that the data is perfectly clustered; whereas, an average SV value approaching 0 suggests the presence of clusters is ambiguous. The optimal number of clusters was determined by the largest positive difference compared to a random distribution of preferred directions.

Axonal distribution analysis

Coronal and parasagittal brain slices containing dLGN were collected from P30 mice ($n = 3$ mice per group). For coronal analysis, three images representative of anterior, middle, and posterior area of dLGN along the anterior-posterior axis, respectively, were selected from each mouse and stained with VGluT2 and GFP. VGluT2 signals were used to demarcate the boundaries of dLGN, allowing masking of neighboring thalamic regions in ImageJ. dLGN images showing expression of GFP were superimposed over three mice and shown as [Figure 2A](#). To assess the distribution of GFP⁺ axons at different depths, dLGN images were re-oriented to align the ventricular surface to vertical line ([Figure S2B top](#)). Signals in the dLGN were subtracted by the averaged pixel value in the neighboring posterior thalamic nuclear group which was used as background control. Every pixel remaining that was greater than 0 was binarized as 1, while those ≤ 0 were assigned as 0. The sum of these pixel values along the vertical line (lateral-to-medial axis) was calculated in MATLAB as cumulative GFP⁺ signals at different depths ([Figure S2B bottom](#)), and binned with $2 \times 2 \mu\text{m}^2$ pixels. To compare the depth distributions of CART-Cre⁺ and BD-CreER⁺ inputs, the summed pixel values were graphed against the distance away from the ventricular surface as dLGN depth ([Figure S2B bottom](#)).

To align with functional recordings of dLGN neurons from parasagittal slices, the distribution of CART-Cre⁺ and BD-CreER⁺ inputs were also analyzed from parasagittal aspect. Three images representative of lateral, middle, and medial area of dLGN along the lateral-medial axis, respectively, were selected from each mouse. dLGN images showing expression of GFP were superimposed over three mice and shown as [Figure 2B](#). For analysis of the distribution of GFP⁺ axons, every pixel within the dLGN was analyzed in the same way as the coronal sections except using the thalamic reticular nucleus as background control. CART-Cre⁺ terminals spanned across the lateral region of dLGN, with increasing density in ventral-posterior areas when moving to medial side of the nucleus ([Figure 2B left](#)). BD-CreER⁺ axons were sparser but also terminated in the ventral-posterior region of dLGN across lateral-to-medial sections ([Figures 2B and S2C](#)). Similar to the analysis in the coronal orientation, one-dimensional line plots were made by calculating vertical maximal projection as summed pixels ($2 \times 2 \mu\text{m}^2$ bins) from anterior-to-posterior of dLGN ([Figure S2C top](#)). The sum of these pixel values along dorsal-ventral axis were graphed against the distance away from the dorsal surface of dLGN ([Figure S2C bottom](#)).

Simulation of ooDSGCs innervation

Two models of CART⁺ ooDSGC subtype innervation patterns were simulated using MATLAB. In Model A, all TC neurons received inputs of varying strengths from ooDSGCs subtypes tuned to two vertical directions (dorsal and ventral motion). In Model B, TC neurons received inputs of varying strengths from just one of the two ooDSGC subtypes. We assumed that the expression of Chr2 was not biased by the strength of a RGC input (and vice versa) and that the responses of TC neurons to the inputs from the two ooDSGC subtypes shared similar cumulative amplitude distribution as those to BD-Cre⁺ inputs at P30. In each simulation for a given TC neuron, the AMPAR amplitude from one (Model B) or from two (Model A) different subtypes of ooDSGCs was randomly chosen from the respective cumulative distribution of BD-Cre⁺ inputs. The simulation was repeated 1000 times. The sum of the AMPAR amplitude of all CART ooDSGC was then tabulated and compared to that of BD ooDSGCs for each model. Simulation with 10,000 repeats yielded the same results in the comparison of cumulative distribution between CART and BD inputs. In other words, for Model A, responses to each ooDSGC subtype were randomly assigned to one TC neuron and summed to obtain the CART AMPAR amplitude, while in Model B, only an input from one of the two subtypes was randomly assigned to the TC neuron. Relevant codes are available (see https://github.com/CCLabmembers/2022_CurrentBiology.git).

Rationale for oEPSC/eEPSC classification

We defined primary drivers of TC neuron firing based on the threshold of oEPSC/eEPSC > 1 for the following reasons. If an individual TC neuron only or mainly receives retinal inputs from CART-Cre⁺ RGCs as primary drivers ($\geq 50\%$ of contribution), one would estimate that the ratio of oEPSC to total retinal drive should be equal to or greater than 0.5. However, we had previously made a similar comparison of the amplitude of oEPSC to eEPSC (optic nerve stimulation) in mice expressing Chr2 in all RGC inputs to dLGN (*Chx10;Chr2*). We found that the peak oEPSC amplitudes are approximately two times greater than eEPSC amplitudes (ratio of oEPSC/eEPSC > 1),⁴¹ consistent with the idea that electrical stimulation in dLGN brain slices underestimates the overall retinal drive due to transected axons. Therefore, we assume the peak eEPSC amplitude represents the lower bound (half) estimate of overall retinal drive onto a TC neuron.

Data analysis and statistics

Electrophysiological data acquisition and offline analysis were performed using custom software in IgorPro (Wave-Metrics, Portland, OR). oEPSC and eEPSC amplitudes were obtained from average traces of 3–5 trials. Data calculation and statistical analysis were conducted using Prism (GraphPad Software), JMP (SAS Institute), and Excel (Microsoft, Redmond, WA). All data sets were evaluated for normality using the Kolmogorov-Smirnov (K-S) test. For nonparametric distributions, the Mann-Whitney or Wilcoxon signed rank test were used for unpaired or paired comparison. For normally distributed data sets, the Student's *t* test was used. K-S test was also used for comparison of distribution curves with (multiple populations) or without (two populations) Bonferroni correction. Box plots indicate the median (line within box), 25–75% quartile range (box), and 10–90% range (whiskers). In violin plots, median is indicated by solid line and quartiles are marked by dashed lines. All data in bar and line graphs were represented as mean ± SEM. For all figures, **p* < 0.05; ***p* < 0.01; ****p* < 0.001.

Current Biology, Volume 32

Supplemental Information

**Functional convergence of on-off
direction-selective ganglion cells
in the visual thalamus**

Qiufen Jiang, Elizabeth Y. Litvina, Héctor Acarón Ledesma, Guanhua Shu, Takuma Sonoda, Wei Wei, and Chinfei Chen

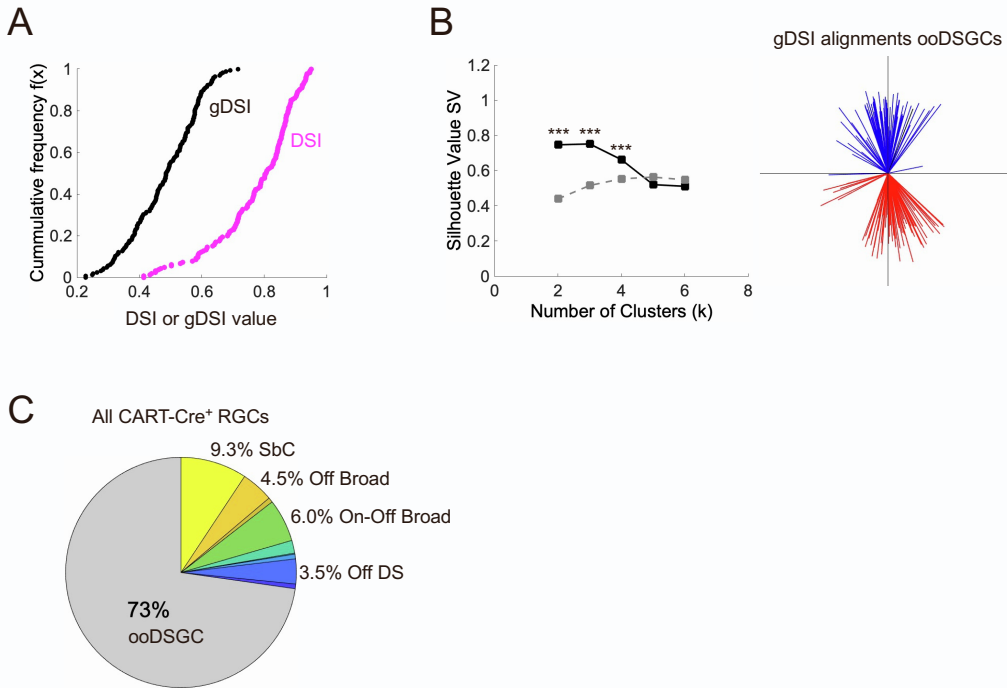


Figure S1. Labelling of ooDSGCs in the retina of *Cart-Cre* mice, related to Figure 1.

(A) Cumulative frequency distribution of direction-selective index (DSI, magenta) and global DSI (gDSI, black). (B) Silhouette analysis for CART-Cre⁺ ooDSGCs. *Left*: Silhouette value (SV) of recorded CART-Cre⁺ RGCs (solid black line) vs. random distribution (grey dashed line) against the number of clusters. Classification by two clusters gives the largest increase in clustering fitness compared to random distribution (***) $p < 0.001$ unpaired t-test). *Right*: Two clusters of CART-Cre⁺ ooDSGCs could be clearly identified that are tuned to dorsal (blue) and ventral (red) motion, respectively. Each line represents vector sum indicating the preferred direction for On-Off cells with $DSI \geq 0.4$. The length of each line represents the value of gDSI. (C) Summary of different RGC types labelled by CART-Cre⁺ RGCs. The majority (73%) of CART-Cre⁺ labeled RGCs were ooDSGCs ($n=246$ cells from 12 retinas, 8 mice). The remaining 27% of CART-Cre⁺ RGCs responded to other visual stimuli, including 9.3% of suppressed-by-contrast (SbC) RGCs, 4.5% of Off broadly-tuned cells (Off Broad), 6.0% of On-Off broadly-tuned cells (On-Off Broad), and 3.5% of Off direction selective (Off DS) cells. Direction selective RGCs are defined as those with $DSI \geq 0.4$, and broadly-tuned cells as those with $DSI < 0.4$ and $OSI < 0.4$ (see STAR Methods).

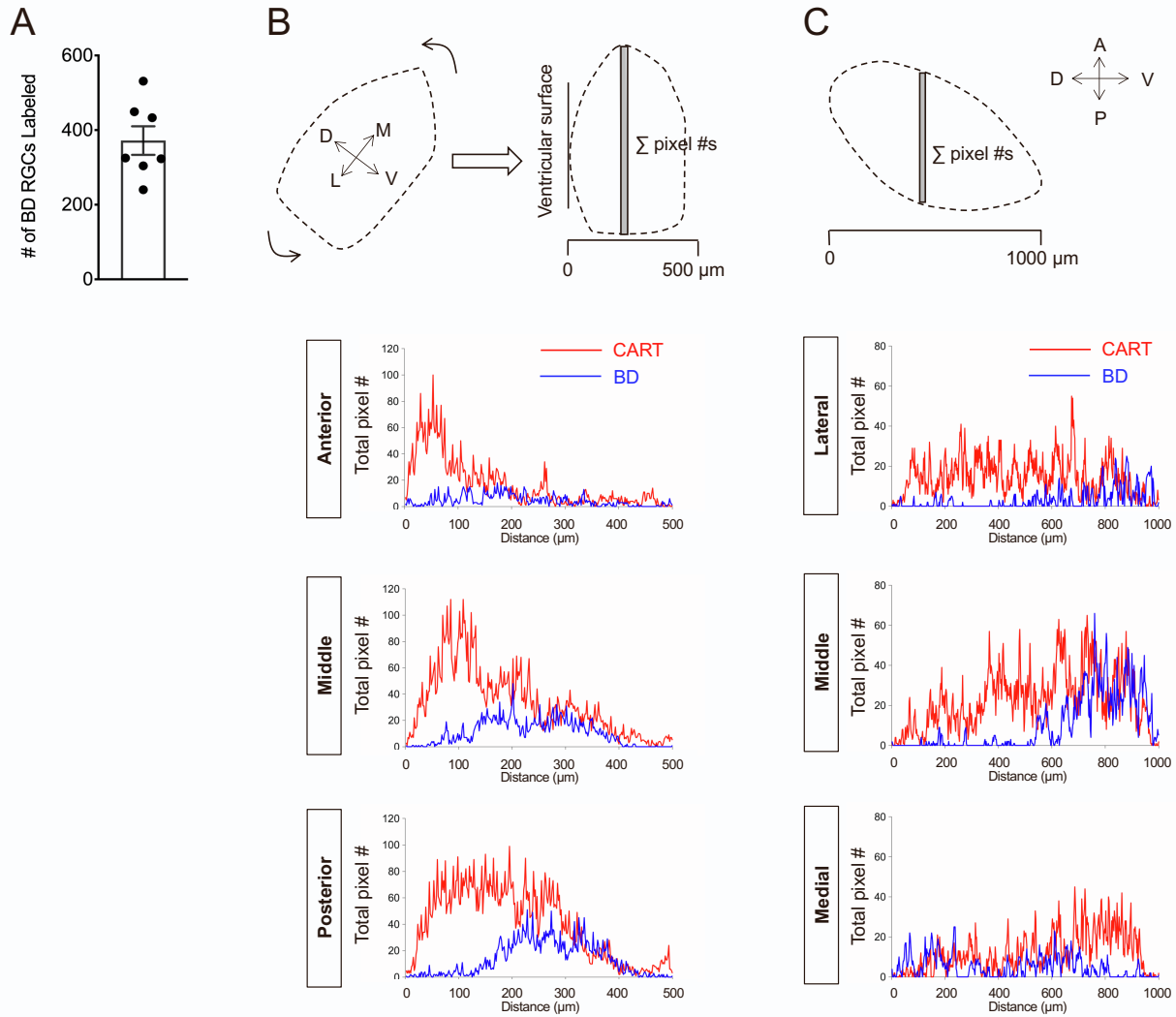


Figure S2. Axonal distribution pattern of CART-Cre⁺ and BD-CreER⁺ inputs in the dLGN, related to Figure 2 and STAR Methods.

(A) Average number of BD-Cre⁺ RGCs labeled in the whole-mount retinas of *BD;ChR2* mice at P30 ($n = 7$ mice). (B) Distribution of CART-Cre⁺/BD-CreER⁺ signals summed along the lateral(L)-to-medial(M) axis as a function of distance away from ventricular surface in coronal slices (see STAR Methods). *Top*: Schematic showing re-orientation of dLGN images to align ventricular surface to vertical line. GFP⁺ signals were calculated by summing up pixels along vertical line (lateral-to-medial axis) to compare peak distribution across the dLGN at different depths along the dorsal-ventral axis. *Bottom*: Line plots of total labeled pixels as a function of dLGN depth from ventricular surface. (C) Same as in B, but for CART-Cre⁺/BD-CreER⁺ signals summed along the anterior(A)-to-posterior(P) projections as a function of distance away from dorsal margin in parasagittal slices. *Top*: Schematic showing summed GFP⁺ signals along A-to-P axis as a function of distance along the dorsal-ventral axis in the dLGN. *Bottom*: Line plots of total pixels labeled plotted against dLGN depth from the dorsal margin.

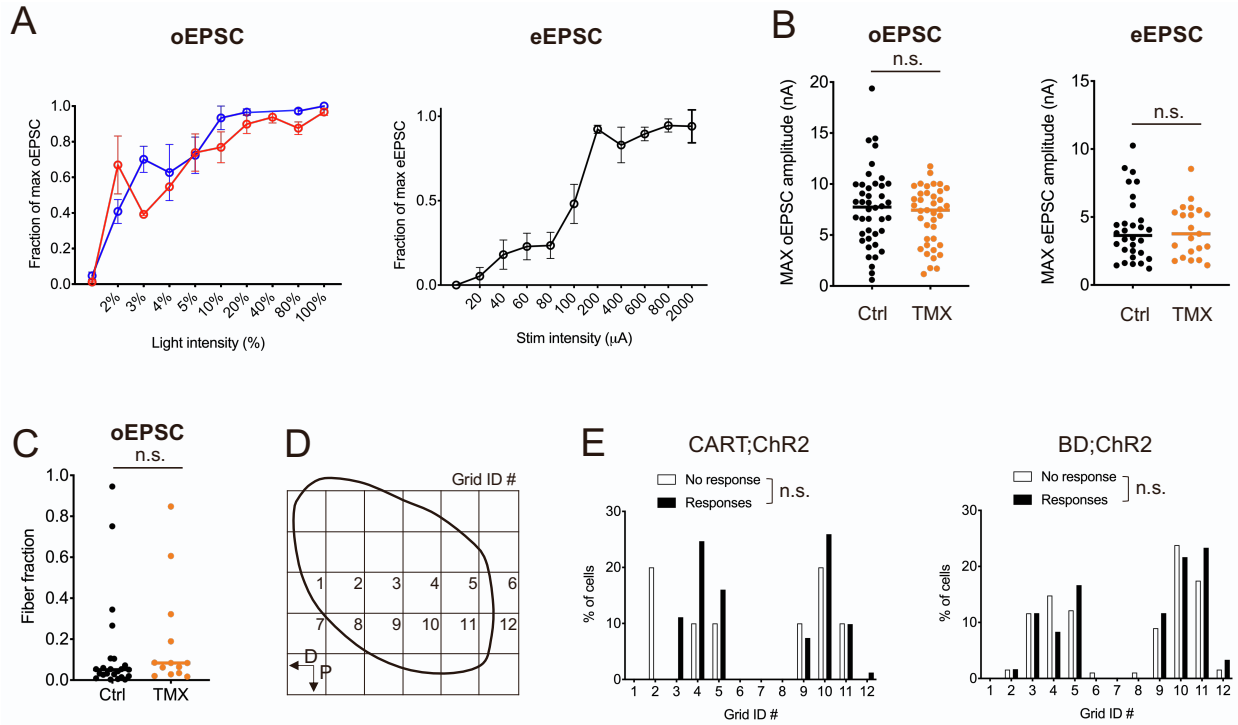


Figure S3. Whole-cell patch clamp recordings in the dLGN, related to Figure 3 and STAR Methods.

(A) Amplitude of AMPAR oEPSC (left, $n = 6$ cells from *Cart;ChR2* mice; $n = 4$ cells from *BD;ChR2* mice) and eEPSC (right, $n = 10$ cells in a separate set of experiments) as a function of light power or electrical stimulation intensity. oEPSC were obtained by activating CART-Cre⁺ (red) or BD-CreER⁺ (blue) inputs with full field light stimulation. (B) Summary of maximum amplitude of AMPAR oEPSCs (left) or eEPSCs (right) recorded from *Chx10;ChR2* mice with or without injection of tamoxifen (TMX) at P0-1. Left: oEPSCs were obtained by stimulating Chx10-Cre⁺ inputs. There is no difference in the average amplitude of oEPSC in mice that received TMX injection (Control (Ctrl): $n = 42$ cells; TMX: $n = 39$ cells; Unpaired t test, $p = 0.29$). Right: eEPSCs amplitudes are not altered in mice that received TMX injection (Ctrl: $n = 30$ cells; TMX: $n = 21$ cells; Mann Whitney test, $p = 0.91$). (C) Fiber fraction of Chx10-Cre⁺ inputs with or without injection of TMX at P0-1. The fiber fraction of Chx10-Cre⁺ inputs after TMX injection was not significantly different from controls (control: 0.13 ± 0.05 , $n = 23$; TMX: 0.19 ± 0.07 , $n = 13$; Mann-Whitney test, $p = 0.15$). (D) Grid map for parasagittal dLGN. The ventral-posterior region of dLGN containing all the recorded neurons was partitioned into 12 grid sections labeled #1-12. (E) Frequency distribution of responsive and non-responsive neurons to CART-Cre⁺ ($n = 93$ cells, left) or BD-CreER⁺ inputs ($n = 318$ cells, right) in the 12 grids. Left: $p = 0.64$ Two-way ANOVA; Right: $p = 0.71$ Two-way ANOVA.

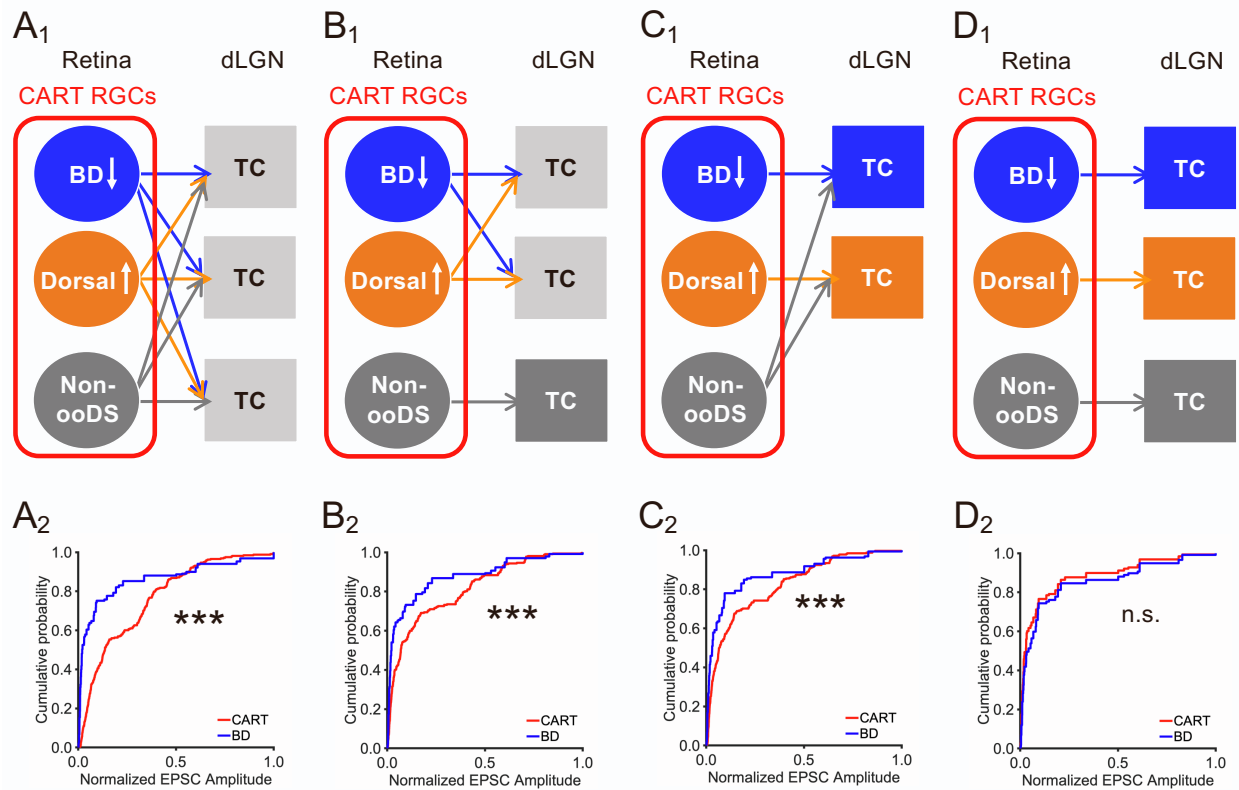


Figure S4. Non-specific labeling of CART-Cre⁺ inputs does not affect simulation results, related to Figure 6 and STAR Methods.

(A₁-D₁) Four simulation models for wiring patterns derived from Figure 6A that consider the label of non-ooDSGC in the CART-Cre⁺ line. A₁-B₁: as in Model A but with CART-Cre⁺ non-ooDSGCs inputs mixing (A₁) or not mixing (B₁) with ooDSGCs; C₁-D₁: as in Model B but with CART-Cre⁺ non-ooDSGCs inputs mixing (C₁) or not mixing (D₁) with ooDSGCs. (A₂-D₂) Simulated normalized cumulative probability curves based on A₁-D₁ models. *** p < 0.001, Kolmogorov-Smirnov test.